Bubbly flow and gas–liquid mass transfer in square and circular microchannels for stress-free and rigid interfaces: CFD analysis

David Mikaelian, Benoît Haut & Benoit Scheid

Microfluidics and Nanofluidics

ISSN 1613-4982

Microfluid Nanofluid
DOI 10.1007/s10404-015-1578-0

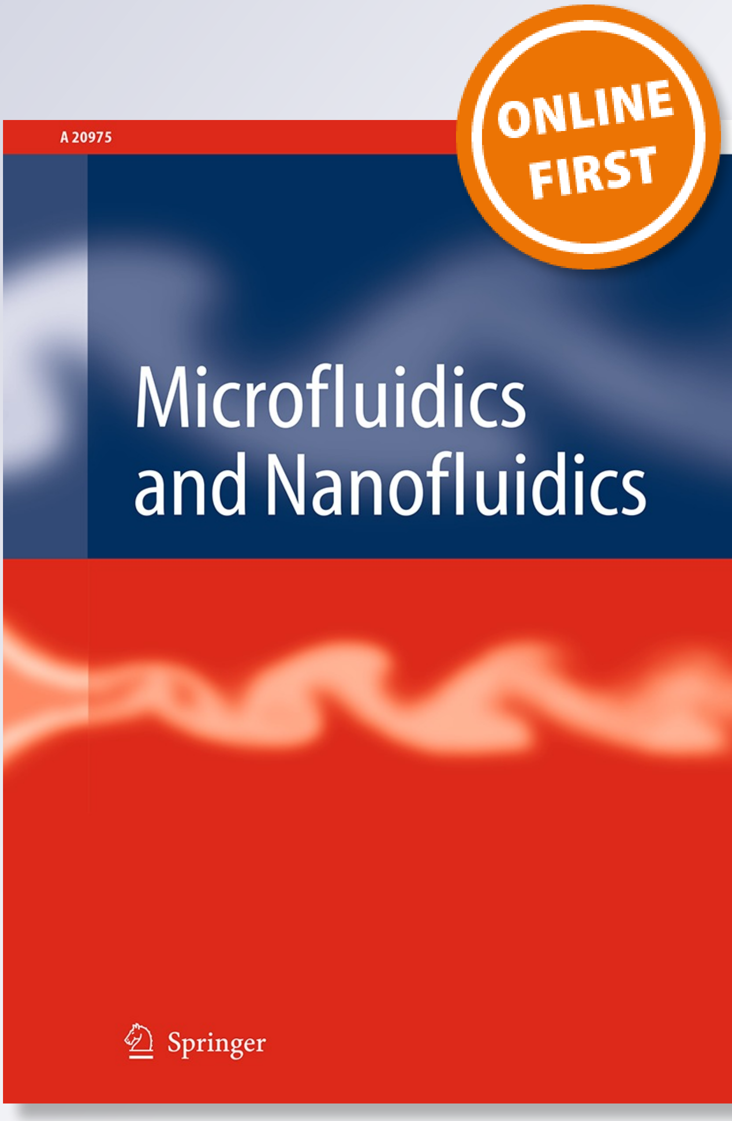

Springer

Your article is protected by copyright and all rights are held exclusively by Springer-Verlag Berlin Heidelberg. This e-offprint is for personal use only and shall not be self-archived in electronic repositories. If you wish to self-archive your article, please use the accepted manuscript version for posting on your own website. You may further deposit the accepted manuscript version in any repository, provided it is only made publicly available 12 months after official publication or later and provided acknowledgement is given to the original source of publication and a link is inserted to the published article on Springer's website. The link must be accompanied by the following text: "The final publication is available at link.springer.com".

Springer

Author's personal copy

Microfluid Nanofluid
DOI 10.1007/s10404-015-1578-0

RESEARCH PAPER

Bubbly flow and gas–liquid mass transfer in square and circular microchannels for stress-free and rigid interfaces: CFD analysis

David Mikaelian[1] · **Benoît Haut**[1] · **Benoit Scheid**[1]

Received: 6 October 2014 / Accepted: 28 March 2015
© Springer-Verlag Berlin Heidelberg 2015

Abstract In this paper, the dynamics of bubbles and the mass transfer between bubbles and the surrounding liquid in square and circular microchannels are investigated, in the bubbly flow regime. For this purpose, a computational fluid dynamics analysis is used to carry out numerical simulations of the liquid flow and the mass transport around a spherical bubble in a square or a circular microchannel, for a stress-free or a rigid gas–liquid interface. The corresponding results are consolidated into correlations to calculate the bubble velocity and the interfacial rate of mass transfer as functions of the control parameters of the system. For each considered case, the flow structure, the concentration field around the bubble and the local interfacial rate of mass transfer are presented and shown to be intricately related.

Keywords Microfluidics · Absorption · Square microchannel · Circular microchannel · Bubbles · Spherical bubbles · CFD

1 Introduction

Nowadays, microfluidic devices are increasingly used because they enable reaching higher yields than classical processes, having a deep control on the operating conditions, employing continuous processes and lowering the risk due to the use of high quantity of hazardous materials (Song et al. 2006; Pamme 2007; Kashid et al. 2011). Microfluidic devices involving gas–liquid two-phase flows in microchannels are widely encountered even though the gas–liquid mass exchange is scarcely addressed in published works.

Gas–liquid two-phase flow patterns in microchannels were investigated by Cubaud and Ho (2004) and by Kim et al. (2011) in square and rectangular microchannels, respectively. In both works, five regimes were reported, depending on the gas and liquid superficial velocities in the microchannel, and named after Cubaud and Ho (2004) as bubbly, wedging, slug, annular and dry flows. Similar regimes were observed in circular channels of 1 mm diameter by Triplett et al. (1999a, b) and in circular microchannels of 100 μm diameter by Kawahara et al. (2002). However, in the experimental setup of Kawahara et al. (2002), the bubbly flow regime could not be observed.

In this paper, we exclusively investigate the bubbly flow regime in square and circular microchannels. The bubbly flow corresponds to discrete spherical bubbles, with diameters smaller than the microchannel hydraulic diameter, moving in a continuous liquid phase. The transition from the slug flow to the bubbly flow was observed in the experiments of Cubaud et al. (2012), when investigating the dissolution of CO_2 bubbles in water in a nearly square microchannel of height $h_C = 100\ \mu\text{m}$ and width $w_C = 87\ \mu\text{m}$. In the work of Cubaud et al. (2012), the bubble size d_C (measured between the tips of the two end-caps of the bubble), its velocity V_B and the total superficial velocity $J_A = \frac{Q_L+Q_G}{h_C w_C}$ were evaluated along the microchannel, Q_L and Q_G being the liquid and gas volumetric flow rates. A correlation to express the ratio V_B/J_A as a function of d_C/w_C was proposed:

$$\frac{V_B}{J_A} = 1 + 1.1 \exp\left[-\left(\frac{d_C}{w_C}\right)^2\right]. \tag{1}$$

✉ David Mikaelian
dmikaeli@ulb.ac.be

1 Transfers, Interfaces and Processes (TIPs), CP 165/67, Université libre de Bruxelles, Av. F. D. Roosevelt 50, 1050 Brussels, Belgium

Published online: 28 April 2015

Author's personal copy

To the best of our knowledge, such a correlation to express V_B/J_A has never been challenged numerically, which is one of the aims of the present work.

The mass transfer between gas bubbles in a microchannel and the surrounding liquid was studied in capillaries and in square and rectangular microchannels by Kashid et al. (2011), Sun and Cubaud (2011), Cubaud et al. (2012) and Shim et al. (2014). These works mainly focused on the slug flow regime. The transition from the slug flow to the bubbly flow was observed in the experiments of Cubaud et al. (2012), as mentioned above, but the mass transfer between the bubbles and the surrounding liquid has not been characterized in the bubbly flow regime.

Additionally, the presence of surface-active contaminants has a great influence on the dynamics and morphology of a bubble in a microchannel, because they modify the boundary conditions at the bubble-liquid interface (Haberman and Morton 1953; Clift et al. 1978). Indeed, the presence of surface-active contaminants "rigidifies" the bubble-liquid interface and can lead to a bubble behavior similar to a rigid body.

In this work, the dynamics of spherical bubbles in square and circular microchannels and the mass transfer between these bubbles and the surrounding liquid are investigated in the bubbly flow regime. As detailed hereafter, two kinds of boundary conditions are considered on the bubble–liquid interface (stress-free and no-slip boundary conditions). In Sect. 2, the problem is presented in terms of the geometry, the modeling assumptions, the equations, the boundary conditions and the dimensional analysis. In Sect. 3, a numerical procedure is developed in order to solve the described problem. In Sect. 4, the results of this numerical procedure are used to establish correlations expressing the velocity of the bubbles and the mass transfer rate between these bubbles and the surrounding liquid as functions of the control parameters of the system. These results are also used to characterize the flow and the mass transport in the vicinity of the bubbles. Conclusions and perspectives are presented in Sect. 5.

2 Problem statement

2.1 Geometry of the microchannel

Gas–liquid bubbly flows in a square microchannel of length L_c and width w and in a circular microchannel of length L_c and diameter a are considered. For each microchannel, a model segment of length L containing, at its center, a single spherical bubble of diameter d is studied. Taking benefit of the symmetries, only a quarter of the segment of the square microchannel is analyzed and the analysis of the flow and the mass transport in the segment of the circular microchannel is reduced to a two-dimensional axisymmetric problem. Sketch of the square or circular microchannel and the model segments of the square (a) and the circular (b) microchannels are presented in Fig. 1, including labels of the boundaries.

In a laboratory reference frame $(\tilde{x}, \tilde{y}, \tilde{z})$, the considered bubble moves along the microchannel at a velocity V_B in the positive $\tilde{x}$ direction in a liquid moving in the same direction. Q_L and Q_G are the liquid and gas volumetric flow rates in the microchannel, respectively. The total superficial velocity is defined as $J_A = (Q_L + Q_G)/A_\Sigma$, with A_Σ the area of the cross section of the microchannel—equal to w^2 in the case of the square microchannel and to $\pi a^2/4$ in the case of the circular microchannel.

In a reference frame (x, y, z) attached to the center of the bubble, the walls of the microchannel move at a velocity V_B in the positive x direction and the liquid enters the considered segment of the microchannel at an average velocity $V_B - J_A$ in the positive x direction.

2.2 Modeling assumptions

An uncompressible Newtonian liquid is considered. It is assumed that the mass transfer between the bubble and the liquid does not affect the density and the viscosity of the liquid. They can therefore be considered as homogeneous and time independent. It is also assumed that the bubble–liquid mass transfer is limited by phenomena taking place in the liquid phase. These are common assumptions in the modeling of bubble–liquid mass transfer (see for instance Ponoth and McLaughlin 2000; Dani et al. 2006; Wylock et al. 2010; Figueroa-Espinoza and Legendre 2010). These two assumptions are in particular valid when the transferred species has a low solubility in the liquid phase (Coulson and Richardson 1991).

The bubble is assumed to be spherical. The validity of this assumption is discussed a posteriori in Sect. 4.2.

Two limiting cases are considered regarding the gas–liquid interface: a rigid interface (i.e., the bubble behaves as a solid sphere) and a stress-free interface (i.e., no viscous stress is exerted by the gas on the liquid). The consideration of these two limiting cases is common in the modeling of bubble–liquid mass transfer (see for instance Magnaudet et al. 1995; Ponoth and McLaughlin 2000; Dani et al. 2006; Wylock et al. 2010; Figueroa-Espinoza and Legendre 2010). Note that a stress-free interface corresponds to a clean interface, with a gas to liquid viscosity ratio tending to zero (see Haut and Colinet 2005).

Considering these different elements, it appears that, in order to characterize the flow field around the bubble and the mass transfer between the bubble and the surrounding

Author's personal copy

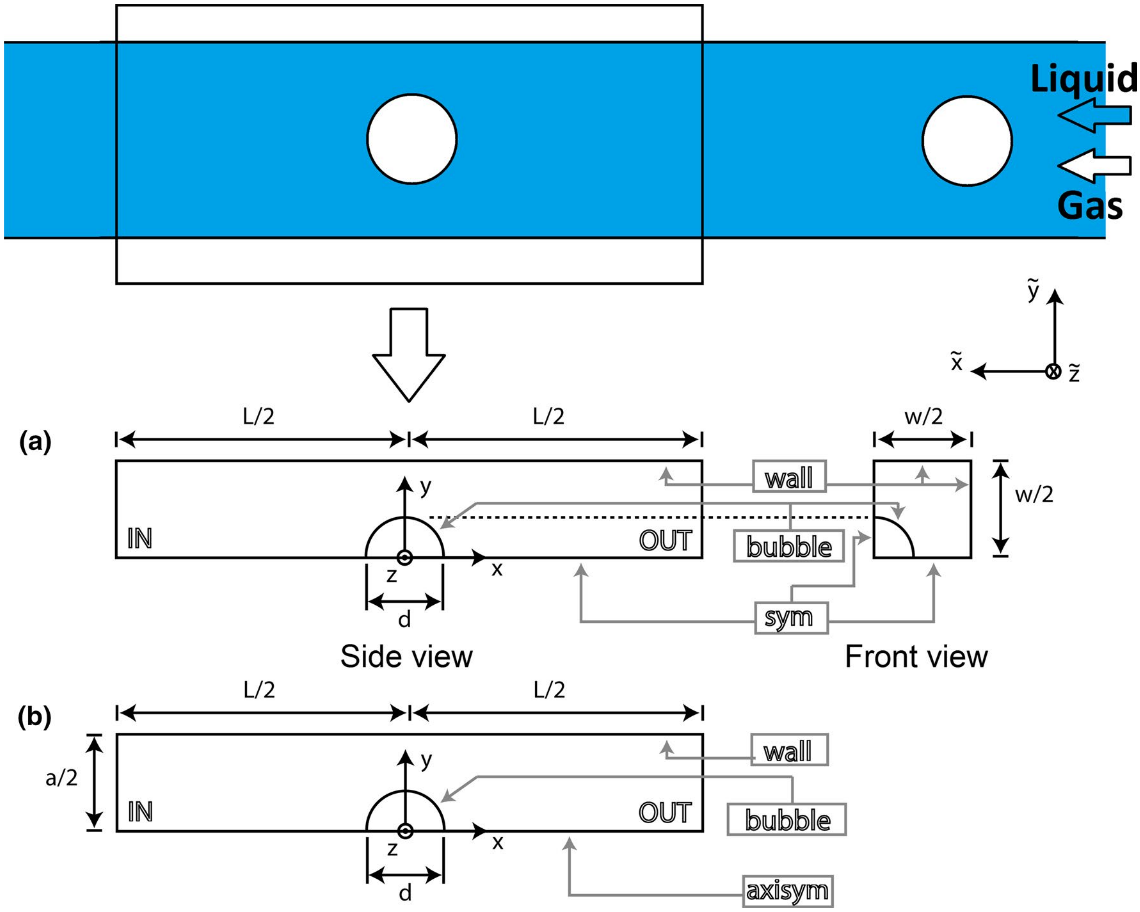

Fig. 1 (*Top*) Sketch of the square or circular microchannel (*Bottom*) **a** model segment of the square microchannel and **b** model segment of the circular microchannel, both represented in a reference frame attached to the center of the bubble (x, y, z). The laboratory reference frame $(\tilde{x}, \tilde{y}, \tilde{z})$ is also represented (see text for other details)

liquid, the momentum and mass transport equations can be solved in the liquid phase only. This assumption is often referred to as the one-sided approach (see for instance Haut and Colinet 2005).

In order to be able to take benefit of the symmetry of the studied system in its modeling (as mentioned in the previous section), it is necessary to assume that the bubble is at the center of the microchannel and that no vortex shedding occurs in the wake of the bubble. The validity of the former assumption is discussed in Sect. 5 and of the latter one in Sect. 4.2. Furthermore, the flow of the liquid and the mass transport in the liquid are considered quasi-steady, i.e., the time derivative in the transport equations in the liquid phase can be set to zero. Such an assumption is valid if the time needed for the establishment of the steady velocity and concentration fields around the bubble in the microchannel ($\approx d/(V_B - J_A)$) is much lower than the characteristic time for the change of the bubble size along the microchannel ($\approx d/k_l$), where k_l is the mass transfer coefficient between the bubble and the liquid (see Eq. 10). As the mass transfer coefficient across the bubble-liquid interface k_l is not known a priori, the validity of this hypothesis is discussed a posteriori in Sect. 4.1.2.

2.3 Equations

According to the assumptions stated in Sect. 2.2, the liquid flow and the mass transport around the bubble in the model microchannel segments of Fig. 1 are analyzed by solving, in the reference frame (x, y, z) attached to the center of the bubble, the continuity, the Navier–Stokes and the mass transport equations, in a stationary state:

$$\nabla \cdot \mathbf{v} = 0, \tag{2}$$

$$\rho(\mathbf{v} \cdot \nabla)\mathbf{v} = -\nabla p + \nabla \cdot \bar{\bar{T}} = -\nabla p + \mu \nabla \cdot \nabla \mathbf{v}, \tag{3}$$

$$\mathbf{v} \cdot \nabla C = D \nabla \cdot \nabla C, \tag{4}$$

with ∇ the gradient operator ($\mathrm{m^{-1}}$), $\mathbf{v}$ the liquid velocity vector ($\mathrm{m\,s^{-1}}$), ρ the density of the liquid ($\mathrm{kg\,m^{-3}}$), p the pressure in the liquid phase (Pa), $\bar{\bar{T}} = 1/2\,\mu(\nabla\mathbf{v} + (\nabla\mathbf{v})^T)$

Author's personal copy

the viscous stress tensor (Pa), μ the dynamic viscosity of the liquid (Pa s), C the concentration of the dissolved gas in the liquid phase ($\mathrm{mol\,m^{-3}}$) and D the corresponding diffusion coefficient ($\mathrm{m^2\,s^{-1}}$).

For the square microchannel, the three-dimensional version of Eqs. 2–4 is solved, while for the circular microchannel, the two-dimensional axisymmetric version of Eqs. 2–4 is solved.

2.4 Boundary conditions

The boundary conditions for the liquid flow and the mass transport are presented in Table 1 for the square and the circular microchannels.

On the bubble surface, two cases are considered: a stress-free interface and a rigid interface, as discussed in the modeling assumptions. The boundary conditions at the stress-free interface are given by

$$\begin{cases} \mathbf{v} \cdot \mathbf{n} = 0, \\ (\bar{\bar{T}} \cdot \mathbf{n}) \cdot \mathbf{t_1} = 0, \\ (\bar{\bar{T}} \cdot \mathbf{n}) \cdot \mathbf{t_2} = 0, \end{cases} \tag{5}$$

where $\mathbf{n}$ is the normal vector to the bubble surface pointing outward the liquid phase and $\mathbf{t_1}$ and $\mathbf{t_2}$ are the tangential vectors to the bubble surface along the principal directions of the bubble surface. These boundary conditions are usually referred to as a "stress-free condition." The boundary conditions at the rigid interface are given by

$$\begin{cases} \mathbf{v} \cdot \mathbf{n} = 0, \\ \mathbf{v} \cdot \mathbf{t_1} = 0, \\ \mathbf{v} \cdot \mathbf{t_2} = 0. \end{cases} \tag{6}$$

These boundary conditions are usually referred to as a "no-slip condition." Thus, four cases are considered in this work, a bubble with either a stress-free or a rigid interface in a square microchannel and a bubble with either a stress-free or a rigid interface in a circular microchannel.

Pseudo-periodic boundary conditions are used for the IN and the OUT planes defined in Fig. 1:

$$\begin{cases} \mathbf{v}_{|x=-L/2} = \mathbf{v}_{|x=L/2}, \\ p_{|x=-L/2} = p_{|x=L/2} + \Delta P, \\ C_{|x=-L/2} = C_{|x=L/2} + \Delta C, \\ \frac{1}{A_\Sigma} \int_{\mathrm{IN}} v_x \, \mathrm{d}S = V_B - J_A, \\ \frac{1}{A_\Sigma} \int_{\mathrm{IN}} C \, \mathrm{d}S = C_{\mathrm{bulk}}, \end{cases} \tag{7}$$

where ΔP and ΔC are, respectively, the pressure and the concentration differences between IN and OUT, and v_x is the x-component of $\mathbf{v}$; ΔP and ΔC are unknown. By using such pseudo-periodic conditions, a chain of bubbles separated by a distance L within the microchannels is actually considered.

2.5 Dimensional analysis

Three dimensionless control parameters can be built to define the system: the ratio between the bubble diameter and the hydraulic diameter of the microchannel, d/d_h, the Reynolds number based on d_h and J_A, $\mathrm{Re}_{J_A} = \frac{\rho d_h J_A}{\mu}$, and the Schmidt number, $\mathrm{Sc} = \frac{\mu}{\rho D}$. The hydraulic diameter is used in order to unify the study of the square and circular microchannels. Indeed, d_h is equal to w for the square microchannel and to a for the circular microchannel. The considered ranges of these three dimensionless parameters are presented in Table 2 and cover a wide range of realistic values for usual bubbly flows in microchannels. In order to cover these ranges of the dimensionless control parameters, the values of d, J_A and D are changed according to Table 2 and the values of d_h, μ and ρ are fixed to 200 µm, 0.5513 mPa s and 791 $\mathrm{kg\,m^{-3}}$, respectively.

Table 1 Boundary conditions for the liquid flow and the mass transport for the square and the circular microchannels, with the boundaries labeled in Fig. 1

Boundaries	Boundary conditions for the liquid flow	Boundary conditions for the mass transport
bubble (see Eqs. 5 and 6)	Spherical and stationary surface with a stress-free condition or a no-slip condition	Imposed interfacial concentration, denoted C_{int}
wall	$\mathbf{v} = (V_B, 0, 0)$	No mass flux across the wall: $\mathbf{n} \cdot \nabla C = 0$
sym	Symmetry planes	Symmetry planes
IN and OUT (see Eq. 7)	Pseudo-periodic conditions with an imposed mass flow rate equal to $(V_B - J_A)\rho A_\Sigma$	Pseudo-periodic conditions with an imposed average concentration only on the plane IN, denoted C_{bulk}
axisym	Symmetry axis	Symmetry axis

Table 2 Ranges of dimensional and dimensionless control parameters

Dimensional control parameters	Dimensionless control parameters
$30\,\mu\mathrm{m} \leq d \leq 150\,\mu\mathrm{m}$	$0.15 \leq d/d_h \leq 0.75$
$0.02\,\mathrm{m\ s^{-1}} \leq J_A \leq 0.1\,\mathrm{m\ s^{-1}}$	$5.74 \leq \mathrm{Re}_{J_A} \leq 28.7$
$1.26\mathrm{x}10^{-9}\mathrm{m^2\ s^{-1}} \leq D \leq 4.58\,\mathrm{x}\,10^{-9}\,\mathrm{m^2\ s^{-1}}$	$152 \leq \mathrm{Sc} \leq 551.3$

Author's personal copy

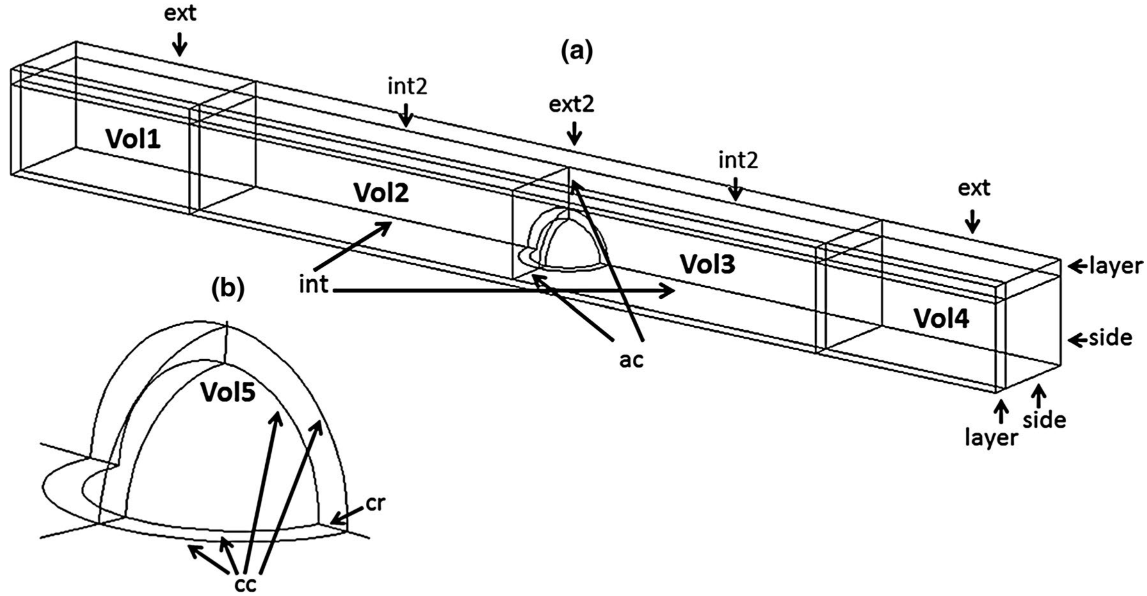

Fig. 2 **a** Three-dimensional geometry and labels of the edges and volumes for the square microchannel segment, **b** zoom on the refined zone around the bubble (*cc* includes all the circular arcs of Vol5). Labels refer to "Square microchannel" in Appendix 1

Two dimensionless variables are defined for the post-processing of the numerical simulations: the ratio of the bubble velocity to the total superficial velocity, V_B/J_A, and the Sherwood number, $\mathrm{Sh} = \frac{k_l d}{D}$, corresponding to the dimensionless mass transfer coefficient. In this work, correlations are established in order to express V_B/J_A and Sh as functions of the three dimensionless control parameters d/d_h, Re_{J_A} and Sc:

$$\frac{V_B}{J_A} = f_1\left(\frac{d}{d_h}, \mathrm{Re}_{J_A}\right), \tag{8}$$

$$\mathrm{Sh} = f_2\left(\frac{d}{d_h}, \mathrm{Re}_{J_A}, \mathrm{Sc}\right). \tag{9}$$

3 Numerical procedure

3.1 Grid

Based on the geometries of the square and circular microchannel segments described in Fig. 1, grids are generated for each value of d/d_h in both types of microchannels, using the software Gambit 2.4. The three-dimensional geometry and the labels of the edges and volumes of the square microchannel are shown in Fig. 2. The mesh is refined around the bubble and next to the walls to ensure that the diffusion boundary layers are correctly captured. For this purpose, an estimation of the thicknesses of the diffusion boundary layers at the wall (δ_{Cw}) and at the bubble surface (δ_{Cb}) can be calculated using $\delta_{\mathrm{Cw}} \sim d_h/\sqrt{\mathrm{Re}_{J_A}\mathrm{Sc}}$ and $\delta_{\mathrm{Cb}} \sim d/\sqrt{\mathrm{Re}_\infty \mathrm{Sc}}$ with $\mathrm{Re}_\infty = \rho(V_B - J_A)d/\mu$. For a given d/d_h, in order to evaluate the smallest δ_{Cw} and δ_{Cb} in all the cases considered in this work, J_A is taken equal to its maximum value of $0.1\ \mathrm{m\ s^{-1}}$ and V_B is taken equal to $2.1 J_A$ (see Eqs. 12–15 in Sect. 4.1.1). At least four layers of cells are placed in the boundary layers. It is a common practice in the numerical simulation of bubble–liquid mass transfer (see for instance Figueroa-Espinoza and Legendre 2010). The details of the meshing procedure in the case of the square microchannel are provided in "Square microchannel" in Appendix 1.

The two-dimensional geometry and the labels of the edges and surfaces of the circular microchannel are shown in Fig. 3. The same labels as in the case of the square microchannel are used for the edges because these edges have the same length and mesh as in the case of the square microchannel. Refined zones are again used around the bubble and next to the walls to ensure that the diffusion boundary layers are correctly captured. The details of the meshing procedure in the case of the circular microchannel are provided in "Circular microchannel" in Appendix 1.

3.2 Solver

For the square microchannel, the equations and boundary conditions defining the problem are solved using the three-dimensional version of the solver Ansys Fluent 14.5 (referred to as Fluent hereafter) with double precision. This solver relies on the finite volume method. For

Author's personal copy

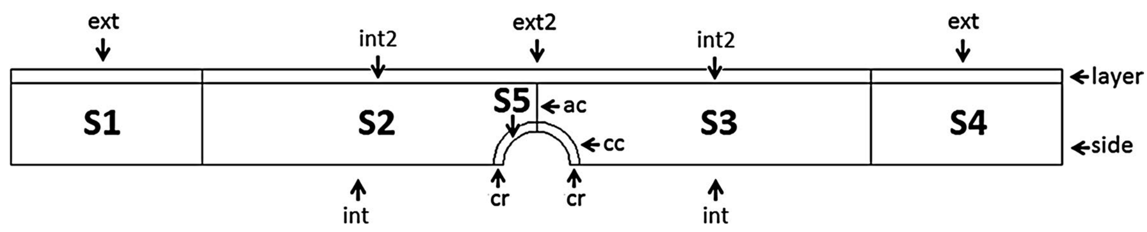

Fig. 3 Two-dimensional geometry and labels of the edges and surfaces used for the circular microchannel segment (*cc* includes all the circular arcs of S5)

the circular microchannel, the two-dimensional axisymmetric version of the solver with double precision is used. For both types of microchannels, second-order upwind discretization schemes are selected for the pressure, the momentum and the concentration, as used, for instance, in the work of Figueroa-Espinoza and Legendre (2010). The pressure–velocity coupling algorithm used is the SIMPLE one, and the gradients are evaluated using the least square cell-based method. The under-relaxation factors are kept at their default values. It has been checked that lowering any of these factors does not lead to a relative modification larger than 0.01 % of the determined x-component of the force exerted by the liquid on the bubble surface (F_x) and of the determined k_l. The iterative procedure is stopped when a relative variation of the computed F_x and k_l lower than 0.001 % is observed in 100 iterations. It has been checked that the obtained results are mesh independent.

3.3 Evaluation of V_B/J_A

For fixed values of the dimensional control parameters d and J_A, V_B is a priori unknown, but it appears in the boundary conditions of the problem. In this work, stationary transport equations are considered. It implies that the x-component of the force exerted by the liquid on the bubble surface (F_x) should be equal to zero. Therefore, to determine V_B for given values of d and J_A, two numerical simulations of the liquid flow are run with two different guesses of the bubble velocity. F_x is evaluated for these two numerical simulations. Then, a linear interpolation of F_x versus the guessed bubble velocity enables calculating V_B, corresponding to $F_x = 0$. In Fig. 4, an example of the determination of V_B is presented, in the case of the bubble with a stress-free interface in the square microchannel; the procedure is identical for the bubble with a rigid interface and in the circular microchannel.

It is worth mentioning that, for each simulation, the length L of the microchannel segment analyzed numerically is set to a value for which it is checked that when L is increased by 200 μm, the relative change in the determined

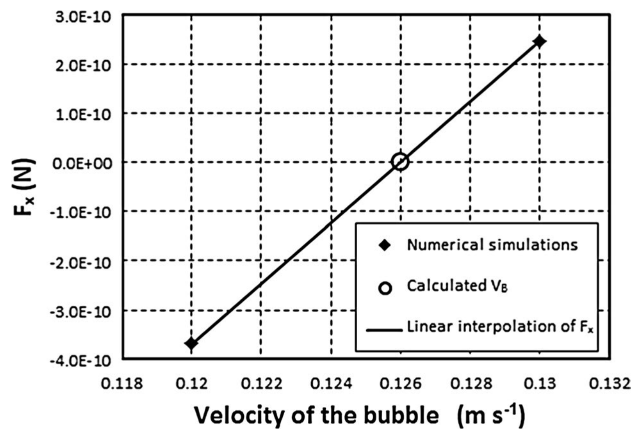

Fig. 4 Example of the calculation of V_B for the bubble with a stress-free interface in the square microchannel, with $d = 50$ μm and $J_A = 0.06\,\mathrm{m\,s^{-1}}$

V_B is lower than 1 %. This procedure ensures that the value of V_B is L-independent, even though the minimum value of L for which it is verified has not been systematically identified.

3.4 Evaluation of Sh

Once V_B is evaluated for given values of d and J_A, numerical simulations of the liquid flow and the mass transport around the bubble can be carried out, leading to the determination of the mass transfer coefficient k_l as follows:

$$k_l = \frac{D \int_{A_b} \mathbf{n} \cdot \nabla C dA_b}{\pi d^2 (C_{\mathrm{int}} - C_{\mathrm{bulk}})}, \tag{10}$$

where A_b is the bubble surface. Knowing k_l, Sh is calculated.

The same procedure as for V_B has been applied here to ensure that the calculated value for Sh is L-independent. The corresponding value of L is found to be larger than the value of L used for V_B, as anticipated from the large values of Sc (see Table 2). The final values of L for each d are given in Table 5.

Author's personal copy

Table 3 Comparison between numerical results obtained using the procedure developed in this work and numerical data and correlations available in the literature

	Microchannel (this work)		Infinite medium (literature)			
	Square	Circular	Haas et al. (1972)	Clift et al. (1978)	Magnaudet et al. (1995)	Wylock et al. (2010)
Stress-free interface						
C_D	1.310	1.332	1.440		1.322	1.424
Sh						
(Sc = 100)	39.48	39.56				39.67
(Sc = 500)	86.31	86.47				86.82
Rigid interface						
C_D	2.715	2.717		2.715	2.707	2.784
Sh						
(Sc = 100)	16.62	16.63		16.85		16.74
(Sc = 500)	27.69	27.71				27.90

These literature data consider a single bubble of diameter d, with either a stress-free interface or a rigid interface, rising in a liquid of infinite extent at a velocity V_B such that $\rho V_B d/\mu = 20$ and with a Schmidt number equal to 100 or 500

3.5 Analysis of the liquid flow and the mass transport around the bubble

Once V_B is evaluated for given values of d, J_A and D, numerical simulations of the liquid flow and the mass transport around the bubble can be carried out using the value of L identified in order to have Sh independent of L. These numerical simulations enable analyzing the velocity field of the liquid, the concentration field of the dissolved gas in the liquid phase and the distribution of the mass transfer rate at the bubble surface.

3.6 Comparison with the literature

In order to assess that the force exerted by the liquid on the bubble and the mass transfer coefficient across its interface are correctly evaluated using the numerical procedure proposed here, the case of a bubble, approaching the unconfined limit, with $d/d_h = 0.02$ in a segment of a square or a circular microchannel of length $L/d = 200$ is considered. The same geometries as in Fig. 1, the same equations as the ones presented in Sect. 2.3 and the same meshing method as the one presented in Sect. 3.1 are used. The same boundary conditions as in Table 1 are used except that the pseudo-periodic conditions are replaced, at the plane IN, by a velocity inlet condition with a velocity $\mathbf{v} = (V_B, 0, 0)$ and $C = C_{\text{bulk}}$ and, at the plane OUT, by an outflow condition with a purely convective mass flux ($\mathbf{n} \cdot \nabla C = 0$). V_B is such that $\rho V_B d/\mu = 20$. The Schmidt number of this system is chosen to be equal to 100 or 500. Such a case is close to the case of a spherical bubble moving in an infinite medium due to the negligible effect of the walls of the microchannel, and thus offers a possibility to assess the numerical procedure by comparison with well-known results available in literature. In Table 3, simulation results, regarding the drag coefficient, $C_D = \frac{8F_x}{\rho V_B^2 \pi d^2}$ in which F_x is evaluated numerically, and the Sherwood number, Sh, of this bubble, are compared with literature data. The correlation given in Haas et al. (1972) is based on numerical data. The results of Magnaudet et al. (1995) and Wylock et al. (2010) were obtained using a finite volume method and a finite element method, respectively. In Clift et al. (1978), the correlation for C_D is given at page 112 and is based on experimental data and the correlation for Sh is given at page 121 and is based on numerical data. The good comparison observed in Table 3 between our results and literature data supports the validity of our numerical procedure.

4 Results and discussion

4.1 Correlations

For the ranges of the control parameters presented in Table 2, numerical simulations of the flow and the mass transport around the bubble with a stress-free interface or a rigid interface in the square or circular microchannel are performed and V_B/J_A and Sh are evaluated as described in Sects. 3.3 and 3.4. The corresponding results are provided in "Appendix 2" and consolidated by correlations as presented below.

4.1.1 Bubble velocity

The following correlation form is proposed to express V_B/J_A as a function of d/d_h:

$$\frac{V_B}{J_A} = 1 + (1 + \lambda) \exp\left[-k_1 \left(\frac{d}{d_h}\right)^{k_2}\right], \tag{11}$$

Author's personal copy

where k_1 and k_2 are fitting parameters and λ is equal to 0.1 for the square microchannel and to 0 for the circular microchannel. Such a correlation form is proposed for the following reasons:

- an analysis of the numerical results demonstrates that V_B/J_A does not depend significantly on Re_{J_A} (see Tables 6, 7, 8, and 9 in "Appendix 2");
- when $d \to 0$, $V_B/J_A \to 2.1$ is expected for the square microchannel and $V_B/J_A \to 2$ is expected for the circular microchannel. Indeed, these values are the theoretical ratios between the maximum and the mean velocities of a laminar one-phase flow in a square and a circular channel, respectively (Bruus 2008);
- when $d \to \infty$, $V_B/J_A \to 1$ is expected, in the limit of which the bubble and the liquid move at the same velocity. Note that this limit is never reached in the bubbly flow regime, which requires $d < d_h$ by definition;
- a similar correlation given in Eq. 1 was successfully used for the fitting of the experimental results of Cubaud et al. (2012), in a nearly square microchannel.

Equation 11 is fitted to the numerical data given in "Appendix 2" by adjusting k_1 and k_2. Then, a fractional number close to the identified value of k_2 is assigned to k_2 and a new fit is done for obtaining the only remaining parameter, k_1. It enables proposing the following correlations for each of the four considered cases:

Stress-free interface:

$$\frac{V_B}{J_A} = 1 + 1.1\exp\left[-\left(\frac{d}{d_h}\right)^5\right] \text{(square)} \tag{12}$$

$$\frac{V_B}{J_A} = 1 + \exp\left[-1.83\left(\frac{d}{d_h}\right)^5\right] \text{(circular)} \tag{13}$$

Rigid interface:

$$\frac{V_B}{J_A} = 1 + 1.1\exp\left[-1.5\left(\frac{d}{d_h}\right)^{9/4}\right] \text{(square)} \tag{14}$$

$$\frac{V_B}{J_A} = 1 + \exp\left[-1.92\left(\frac{d}{d_h}\right)^{9/4}\right] \text{(circular)} \tag{15}$$

Note that these correlations are strictly valid for a chain of bubbles in the ranges of control parameters given in Table 2, which are $0.15 \le d/d_h \le 0.75$ and $5.74 \le \mathrm{Re}_{J_A} \le 28.7$. It is observed in these correlations that, when d/d_h decreases, V_B/J_A increases in each case due to the decreasing influence of the walls on the bubbles.

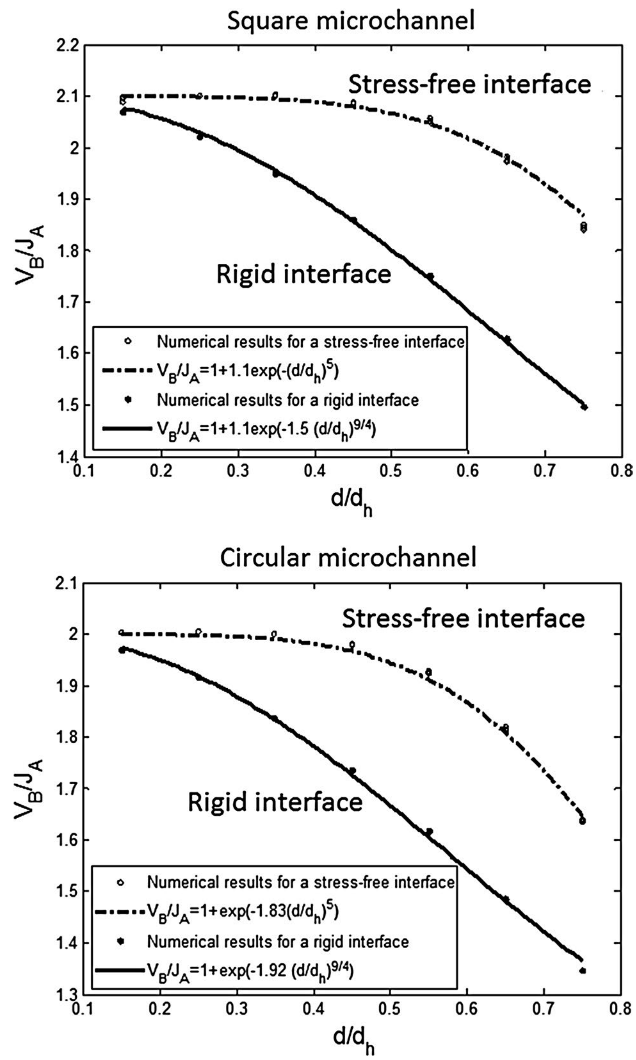

Fig. 5 Values of V_B/J_A computed with Eqs. 12–15 plotted together with the numerical results of V_B/J_A in the cases of the bubble with a stress-free or a rigid interface in the square or circular microchannel

In Fig. 5, the correlations given in Eqs. 12–15 are plotted together with the numerical data given in "Appendix 2."

The correlations to calculate V_B/J_A in the case of the square microchannel can be compared with the experimental data of Cubaud et al. (2012), as presented in Fig. 6. In the work of Cubaud et al. (2012), V_B/J_A and d are measured for CO_2 bubbles dissolving into water in a rectangular microchannel of width w_C and height h_C, which gives $d_h = \frac{2w_C h_C}{w_C + h_C}$. Only the parts of the experiments where $d/d_h \le 0.75$ are considered for comparison. Furthermore, it is assumed that the correlations given in Eqs. 12 and 14 (established for the square microchannel) are still valid for a rectangular microchannel, provided its aspect ratio remains close to unity as it is the case here with $w_C/h_C = 0.87$. As it can be seen in Fig. 6, the case of the bubble with a stress-free interface overestimates the experimental results, while the case of the bubble with a rigid interface underestimates them. This

Author's personal copy

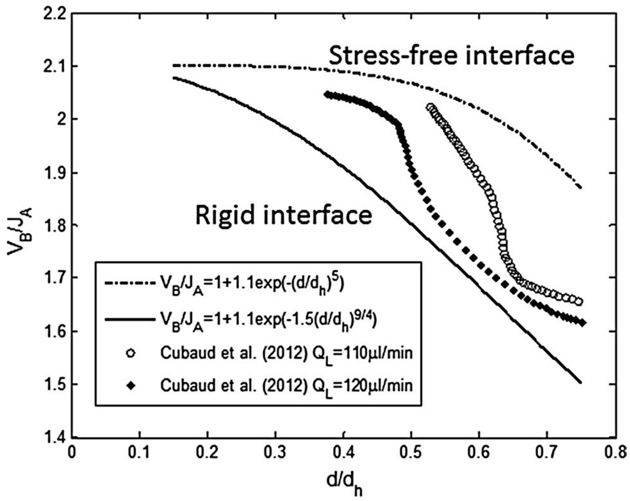

Fig. 6 Comparison between the values of V_B/J_A computed with Eqs. 12 and 14 and the experimental data of Cubaud et al. (2012)

observation suggests that the liquid phase in the experiments of Cubaud et al. (2012) could be contaminated, which invalidates both the stress-free and the no-slip conditions at the bubble surface and leads to values of V_B/J_A between the two limiting values obtained by considering these boundary conditions. The bubble velocity V_B is lower for a bubble with a rigid interface than for a bubble of the same d/d_h with a stress-free interface, because the friction resulting from the no-slip condition in the case of a bubble with a rigid interface slows down the bubble. The fact that V_B/J_A depends on the flow rate in the experiments but not in the correlations for the two limiting cases could also be attributed to the presence of contaminants, which would continuously modify the boundary condition at the bubble surface during the bubble dissolution and hence the flow structure around the bubble. This crucial role of trace impurities on the motion of bubbles has already been shown by Ratulowski and Chang (1990) in the slug flow regime. Stebe and Barthès-Biesel (1995) have further shown in the slug flow regime that the transition from a rigid to a stress-free bubble interface is controlled by adsorption–desorption processes, which are obviously present on a bubble dissolving along a microchannel as the surfactant concentration should vary with both the size of the bubble and its elapsed time inside the microchannel, hence with its position. Recently, Champougny et al. (2015) have also shown that the rigidity of a gas–liquid interface is not an intrinsic property of a surfactant solution, but a function of its dynamical behavior. These considerations are consistent with the observations of the results of Cubaud et al. (2012) plotted in Fig. 6, namely that the rigidity of the bubble surface depends on both the size of the bubble and the liquid flow rate. This is further discussed in Sect. 5.

4.1.2 Interfacial mass transfer

The following correlation form is proposed to express Sh as a function of d/d_h, Re_{J_A} and Sc:

$$\mathrm{Sh} = 2 + k_3 \mathrm{Re}^{k_4} \mathrm{Sc}^{k_5} \left(\frac{d}{d_h}\right)^{k_6}, \tag{16}$$

where k_3, k_4, k_5 and k_6 are fitting parameters and where Re is defined as $\mathrm{Re} = \mathrm{Re}_{J_A} \frac{V_B}{J_A} \frac{d}{d_h} = \frac{\rho V_B d}{\mu}$. Similar correlations were proposed by Levich (1962) to express Sh for low Reynolds number flows around a single sphere with a stress-free or a rigid interface in an infinite medium:

Stress-free interface:

$$\mathrm{Sh} = 2 + 0.6515\,\mathrm{Re}^{1/2}\mathrm{Sc}^{1/2} \quad \text{(infinite medium)} \tag{17}$$

Rigid interface:

$$\mathrm{Sh} = 2 + 0.991\,\mathrm{Re}^{1/3}\mathrm{Sc}^{1/3} \quad \text{(infinite medium)} \tag{18}$$

The factor d/d_h is included in Eq. 16 to take into account the wall effects.

Equation 16 is fitted to the numerical data given in "Appendix 2" by adjusting k_3, k_4, k_5 and k_6. Then, fractional numbers close to the identified values of k_4 and k_5 are assigned to k_4 and k_5 and a new fit is done for obtaining the two remaining parameters, k_3 and k_6. A number close to the identified value of k_6 is then assigned to k_6 and a new fit is done for obtaining the only remaining parameter, k_3. It enables proposing the following correlations for each of the four cases of this work:

Stress-free interface:

$$\mathrm{Sh} = 2 + 3\,\mathrm{Re}^{1/3}\mathrm{Sc}^{1/3}\frac{d}{d_h} \quad \text{(square)} \tag{19}$$

$$\mathrm{Sh} = 2 + 2\,\mathrm{Re}^{2/5}\mathrm{Sc}^{2/5}\frac{d}{d_h} \quad \text{(circular)} \tag{20}$$

Rigid interface:

$$\mathrm{Sh} = 2 + 1.6\,\mathrm{Re}^{1/3}\mathrm{Sc}^{1/3}\frac{d}{d_h} \quad \text{(square)} \tag{21}$$

$$\mathrm{Sh} = 2 + 1.8\,\mathrm{Re}^{1/3}\mathrm{Sc}^{1/3}\frac{d}{d_h} \quad \text{(circular)} \tag{22}$$

Note that these correlations are strictly valid for a chain of bubbles in the ranges of control parameters given in Table 2, which are $0.15 \le d/d_h \le 0.75$, $5.74 \le \mathrm{Re}_{J_A} \le 28.7$ and $152 \le \mathrm{Sc} \le 551.3$. Nevertheless, as these correlations have been constructed such that $\mathrm{Sh} \to 2$ as $d \to 0$ or $\mathrm{Re} \to 0$, which corresponds to the pure diffusion limit, we expect these correlations to be also valid for $d/d_h < 0.15$.

Author's personal copy

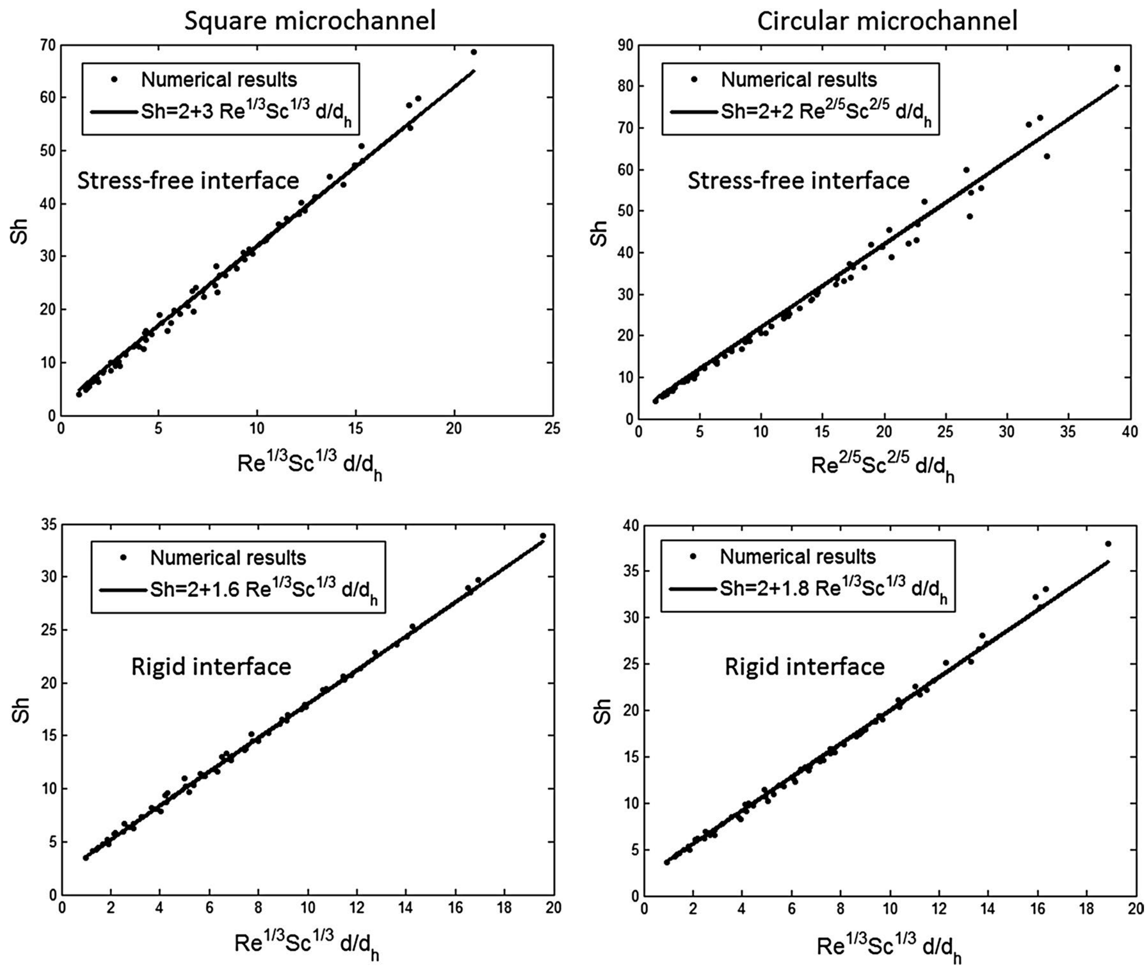

Fig. 7 Values of Sh computed with Eqs. 19–22 plotted together with the numerical results of Sh in the cases of the bubble with a stress-free or a rigid interface in the square or circular microchannel

In Fig. 7, the correlations given in Eqs. 19–22 are plotted together with the numerical data given in "Appendix 2."

Experimental data allowing to evaluate Sh in the bubbly flow regime are not available in literature, but the evolution of the size of a bubble, in the bubbly flow regime, was monitored along a nearly square microchannel in the work of Cubaud et al. (2012), as already mentioned. Therefore, in order to assess the validity of the correlations given in Eqs. 19 and 21, these correlations could be included in a model for the dissolution of spherical bubbles along a square microchannel in the bubbly flow regime, whose results for the evolution of the bubble size along the microchannel could then be compared with the experimental data of Cubaud et al. (2012). This is beyond the scope of the present work and is presented in a separate work (Mikaelian et al. 2015).

It is worth mentioning that, in the case of the bubble with a rigid interface, the exponents of Re and Sc in the correlations for Sh are the same in the square and circular microchannels (Eqs. 21 and 22) and in an infinite medium (Eq. 18), while such a parallelism is not observed in the case of the bubble with a stress-free interface. For the bubble with a stress-free interface, if only the numerical simulations with d/d_h lower than 0.45 are considered, once Eq. 16 is fitted to the numerical data of "Appendix 2," the values of the exponents of Re and Sc approach 1/2, which suggests that the exponents 1/3 and 2/5 in Eqs. 19 and 20 are certainly due to wall effects.

The quasi-steady state assumption mentioned in Sect. 2.2 is valid if $d/(V_B - J_A) \ll d/k_l$, which is equivalent, in dimensionless form, to $\mathrm{Sh}/(\mathrm{Re}_\infty \mathrm{Sc}) \ll 1$, with $\mathrm{Re}_\infty = \mathrm{Re} - \mathrm{Re}_{J_A} d/d_h$. Using the results presented in "Appendix 2," it can be calculated that, for the conditions considered in this work, the largest value of $\mathrm{Sh}/(\mathrm{Re}_\infty \mathrm{Sc})$ is 0.064, which thus supports the quasi-steady state assumption.

Author's personal copy

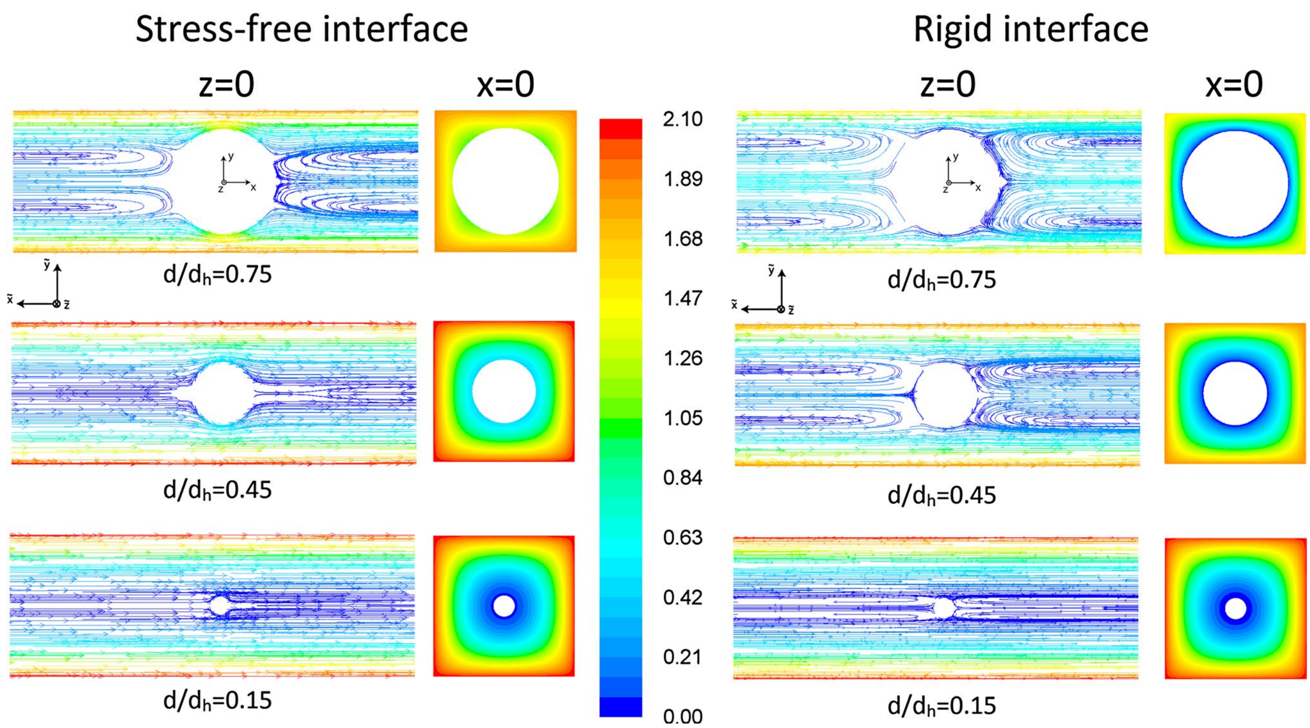

Fig. 8 Pathlines (*colored* by the dimensionless velocity magnitude) around the bubble, for various d/d_h, with a stress-free or a rigid interface, in the symmetry plane $z = 0$ of the square microchannel and contours of the dimensionless velocity magnitude in the plane $x = 0$, for $\mathrm{Re}_{J_A} = 28.7$ (color figure online)

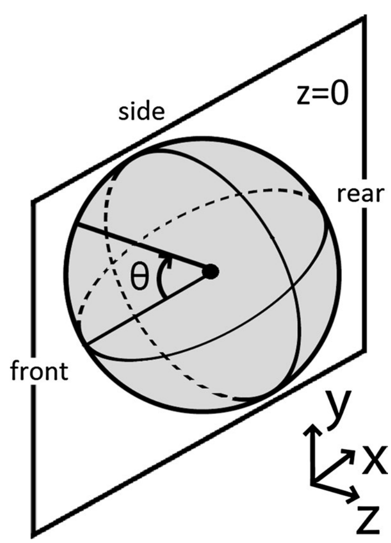

Fig. 9 Intersection between the bubble surface and the plane $z = 0$, with • the center of the circle resulting from this intersection, and definition of the angle θ

4.2 Liquid flow

In Fig. 8, pathlines in the symmetry plane $z = 0$ of the square microchannel and contours of the dimensionless velocity magnitude in the plane $x = 0$ are presented for various d/d_h, with $\mathrm{Re}_{J_A} = 28.7$ and with either a stress-free or a rigid interface. The dimensionless velocity magnitude is defined as the norm of the liquid velocity in the moving reference frame (x, y, z) divided by J_A.

In order to analyze the liquid flow around the bubble in the symmetry plane $z = 0$ of the square or circular microchannel, the intersection of this plane and the bubble surface is used and the angle θ (comprised between 0 and π) is defined as presented in Fig. 9. In this work, the zone of the bubble surface where $\theta \approx 0$ is called the front of the bubble, the zone where $\theta \approx \pi/2$ is called the side of the bubble and the zone of the bubble where $\theta \approx \pi$ is called the rear of the bubble.

As it can be seen in Fig. 8 in the case of the bubble with a stress-free interface, when d/d_h increases, a recirculation appears between two successive bubbles, as in a slug flow (Kashid et al. 2011). It can be explained by the fact that the bubble moves (in the positive $\tilde{x}$ direction) with a velocity V_B higher than J_A. For $d/d_h = 0.15$, the liquid is able to go from the front of the bubble to its rear. When d/d_h increases, the liquid cannot get around the bubble and a recirculation is generated. When such a recirculation is present between two successive bubbles, the liquid flow around one of these bubbles is influenced by the other one. This influence disappears when d/d_h is sufficiently small. In the case of the bubble with a rigid interface, a

Author's personal copy

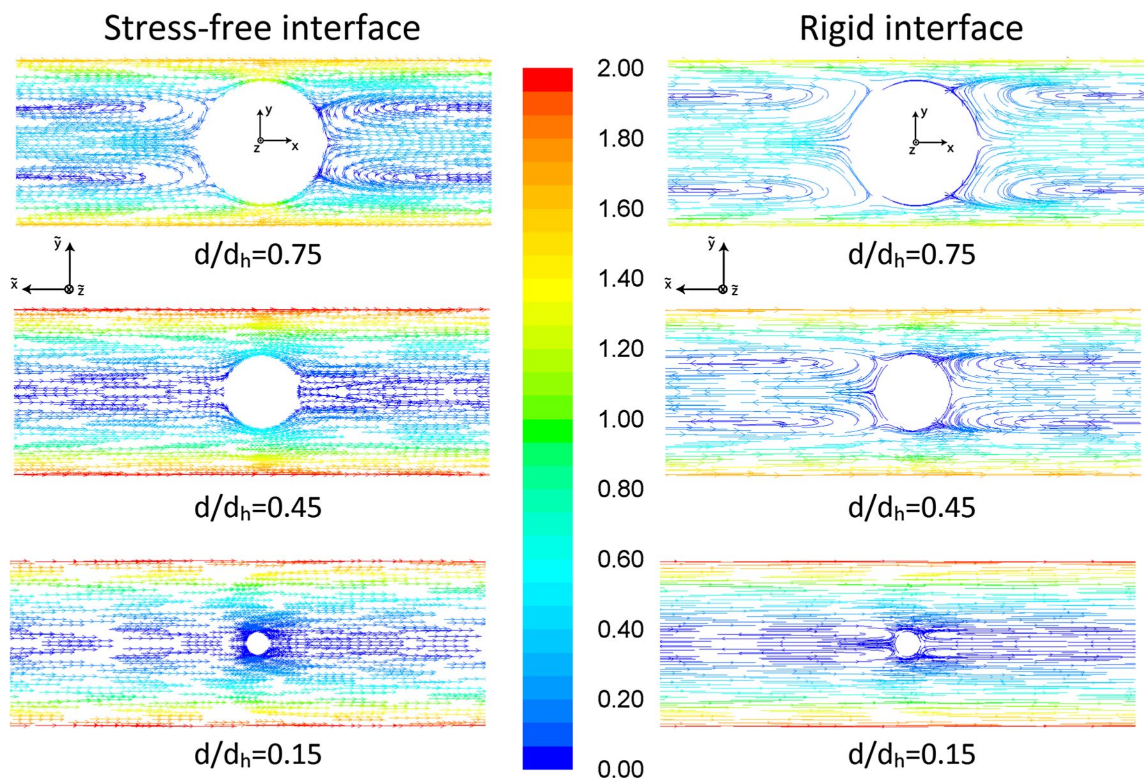

Fig. 10 Pathlines (*colored* by the dimensionless velocity magnitude) around the bubble, for various d/d_h, with a stress-free or a rigid interface, in the symmetry plane $z = 0$ of the circular microchannel, for $\mathrm{Re}_{J_A} = 28.7$ (color figure online)

recirculation is present between two successive bubbles for all the considered values of d/d_h, because, in addition to the fact that the liquid flow cannot get around the bubble as d/d_h gets closer to unity, the liquid is carried by the front of the bubble due to the no-slip condition at the bubble surface. This second reason explains why, for low values of d/d_h, a recirculation is still present in the case of the bubble with a rigid interface, while it disappears in the case of the bubble with a stress-free interface.

Figure 8 shows that, in the case of the bubble with a stress-free interface, the dimensionless velocity magnitude is minimal at the front and at the rear of the bubble surface, while it is maximal on the side of the bubble surface. In the case of the bubble with a rigid interface, the dimensionless velocity magnitude is equal to zero on the bubble surface and is the highest in the vicinity of the bubble side. In both cases, the dimensionless velocity magnitude is equal to V_B/J_A on the walls of the microchannel.

The flow field around the bubble with a stress-free or a rigid interface in the circular microchannel appears to be quite similar to the one obtained in the square microchannel, as shown in Fig. 10 for various d/d_h and $\mathrm{Re}_{J_A} = 28.7$. However, a notable difference can be observed between the flow fields in both types of microchannel. A meticulous analysis of the contours of the dimensionless velocity magnitude in the plane $x = 0$ for the bubble with a stress-free or a rigid interface in the square microchannel (see Fig. 8) for $d/d_h = 0.75$ shows the presence of an azimuthal asymmetry in the liquid flow close to the bubble surface. Indeed, the dimensionless velocity magnitude close to the bubble surface is higher in the symmetry planes $y = 0$ and $z = 0$ than in between them. This can be explained by the fact that the bubble surface is the closest to the walls of the microchannel in these symmetry planes. Such an azimuthal asymmetry close to the bubble surface is obviously not observed in the circular microchannel. This azimuthal asymmetry disappears when d/d_h decreases because the influence of the walls decreases, as it can be observed in the plane $x = 0$ for $d/d_h = 0.15$ in Fig. 8.

It has been assumed here that the bubble is spherical. For the bubble with a rigid interface, this hypothesis is obviously appropriate, but it has to be evaluated for the bubble with a stress-free interface. To that aim, the capillary number Ca and the Weber number We can be evaluated. The capillary number compares the viscous forces which tend to deform the bubble-liquid interface and the surface tension forces which tend to keep it spherical. By using an analogy with a shear flow for the liquid flow around the bubble (Rust and Manga 2002), Ca can be calculated as $\mathrm{Ca} = \mu G d/\sigma$, with G the shear rate acting on the bubble (that can be calculated

Author's personal copy

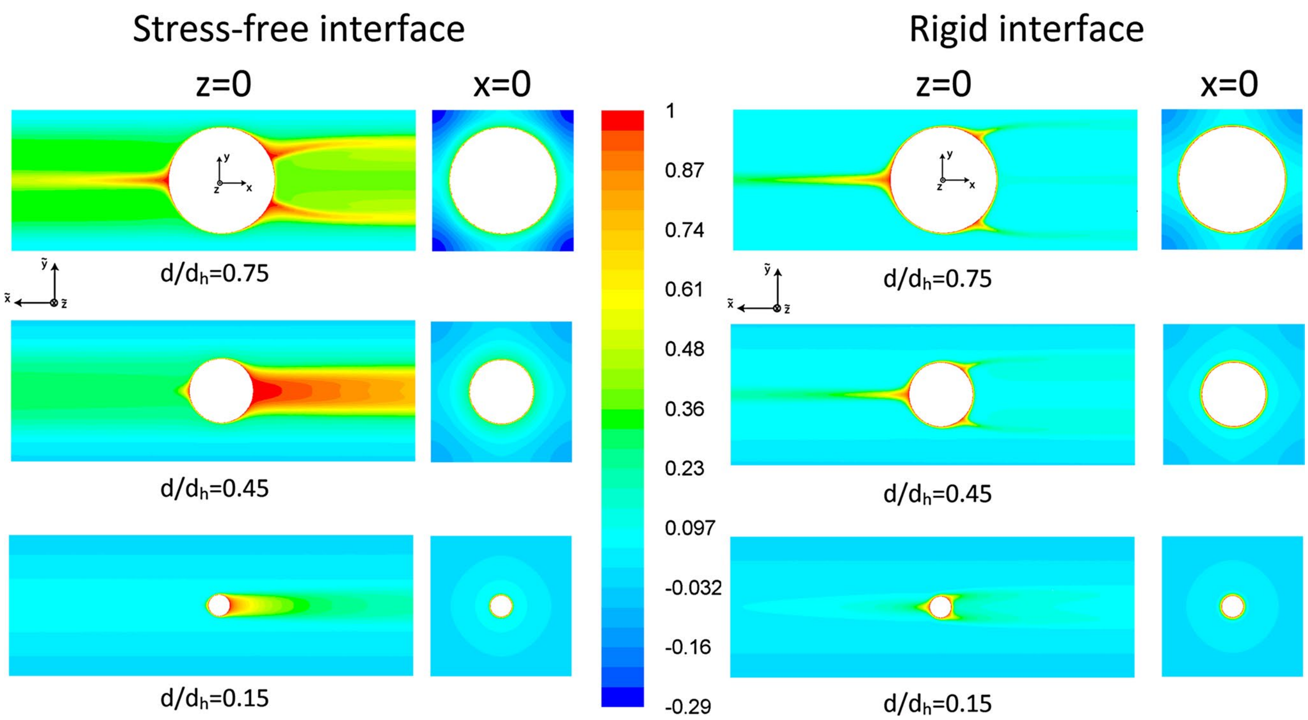

Fig. 11 Dimensionless concentration field C^* around the bubble, for various d/d_h, with a stress-free or a rigid interface, in the symmetry plane $z = 0$ and in the plane $x = 0$ of the square microchannel for $\mathrm{Re}_{J_A} = 28.7$ and $\mathrm{Sc} = 551.3$ (color figure online)

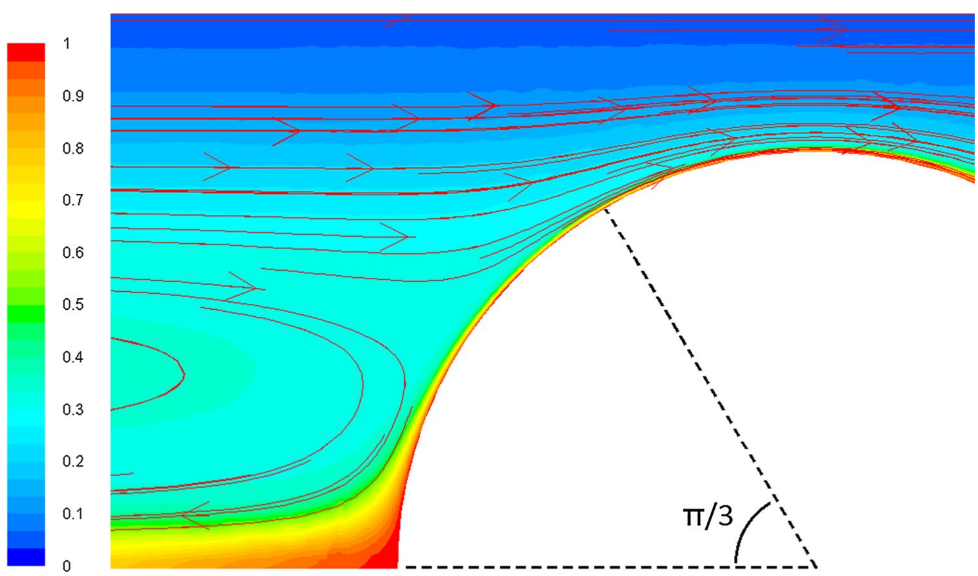

Fig. 12 Superposition of the pathlines and the dimensionless concentration field C^* in the vicinity of the bubble with a stress-free interface in the symmetry plane $z = 0$ of the square microchannel for $d/d_h = 0.75$, $\mathrm{Re}_{J_A} = 28.7$ and $\mathrm{Sc} = 551.3$ (color figure online)

with the simulated velocity field) and σ the surface tension of the gas–liquid interface. The Weber number compares the inertial forces, which tend to deform the bubble-liquid interface and the surface tension forces. By using an analogy with a bubble moving in an infinite medium, We can be calculated as $\mathrm{We} = \frac{\rho (V_B - J_A)^2 d}{\sigma}$. It has been checked that, for the cases considered in this work, Ca is always lower than 0.03 and We is always lower than 0.07, which support the hypothesis of spherical bubbles.

As mentioned in Sect. 2.2, it is assumed that no vortex shedding occurs in the wake of the bubble. This assumption was checked in the conditions for which vortex shedding is the most likely to occur. For this purpose, according to the range of values of the dimensionless numbers used in this work (see Table 2), a three-dimensional unsteady numerical simulation of the liquid flow was carried out for the complete square microchannel segment containing at its center the bubble with a rigid interface, with $d/d_h = 0.75$

Author's personal copy

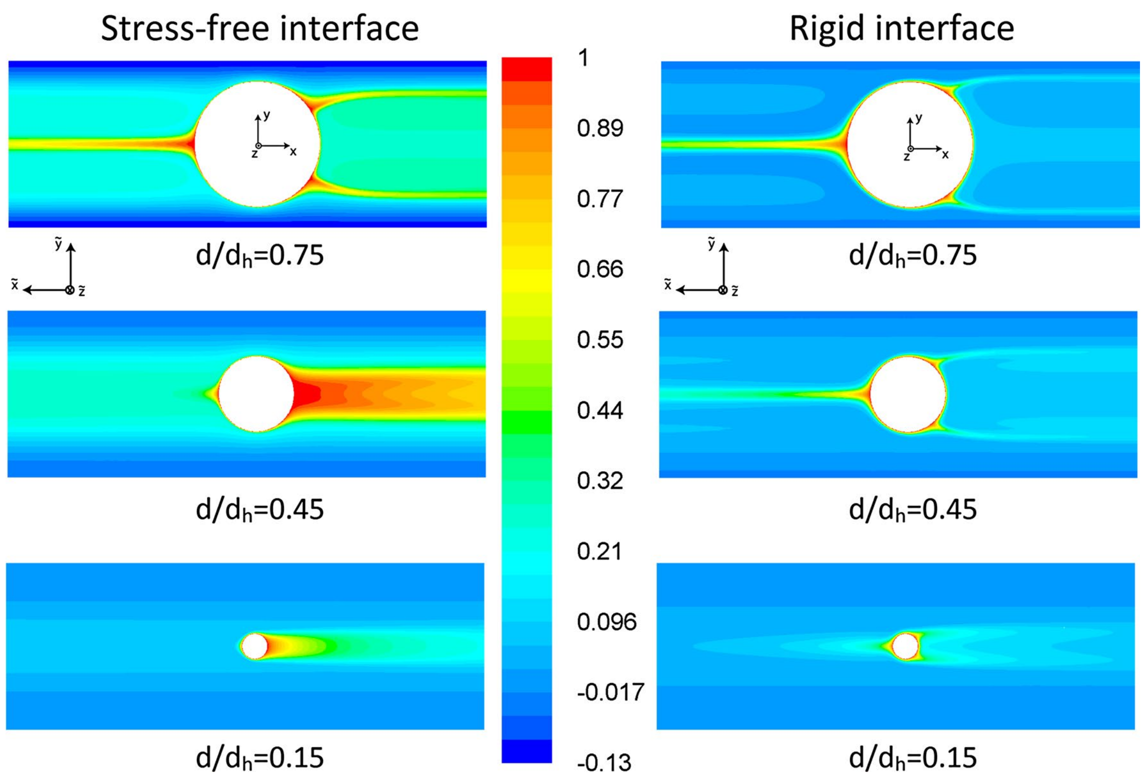

Fig. 13 Dimensionless concentration field C^* around the bubble, for various d/d_h, with a stress-free or a rigid interface, in the symmetry plane $z = 0$ of the circular microchannel for $\mathrm{Re}_{J_A} = 28.7$ and $\mathrm{Sc} = 551.5$ (color figure online)

and $\mathrm{Re}_{J_A} = 28.7$. The simulation results showed no vortex shedding and matched the ones obtained when considering only a quarter of the microchannel segment and a steady state.

4.3 Concentration fields of the dissolved gas in the liquid phase

In Fig. 11, the dimensionless concentration field of the dissolved gas in the liquid phase is presented in the symmetry plane $z = 0$ and in the plane $x = 0$ of the square microchannel for various d/d_h, with $\mathrm{Re}_{J_A} = 28.7$, $\mathrm{Sc} = 551.3$ and either a stress-free or a rigid interface. A dimensionless concentration $C^* = \frac{C - C_{\mathrm{bulk}}}{C_{\mathrm{int}} - C_{\mathrm{bulk}}}$ is presented in Fig. 11. It enables making the analysis of the concentration fields independent of C_{int} and C_{bulk}. For $C = C_{\mathrm{int}}$, $C^* = 1$ and for $C = C_{\mathrm{bulk}}$, $C^* = 0$.

The concentration field C^* around the bubble is significantly influenced by the flow field as it can be seen by comparing Figs. 8 and 11, especially at the stagnation points on the bubble surface observed for $d/d_h = 0.75$ in the case of the bubble with a stress-free interface and for all the considered values of d/d_h in the case of the bubble with a rigid interface.

The thickness of the diffusion boundary layer appears to be minimum at a position on the bubble surface characterized by $\theta \approx \pi/3$, as shown in Fig. 12, where the superposition of the pathlines and the dimensionless concentration field is presented in the vicinity of the bubble with a stress-free interface in the symmetry plane $z = 0$ of the square microchannel for $d/d_h = 0.75$, $\mathrm{Re}_{J_A} = 28.7$ and $\mathrm{Sc} = 551.3$. This minimum value results from an interaction between the growth of the thickness of the diffusion boundary layer when θ increases and the increase of the liquid velocity when θ increases, due to the decreasing area of the cross section available for the liquid flow, with a minimum value of this area at $\theta = \pi/2$. As the thickness of the boundary layer is minimum at a position on the bubble surface characterized by $\theta \approx \pi/3$, the mass transfer between the bubble and the surrounding liquid is expected to be the highest in this region.

The C^* field around the bubble with a stress-free or a rigid interface in the circular microchannel appears to be quite similar to the one obtained in the square microchannel, as shown in Fig. 13 for various d/d_h, $\mathrm{Re}_{J_A} = 28.7$ and $\mathrm{Sc} = 551.3$.

It is worth mentioning that the boundary condition imposed at the plane IN is that the average concentration of the dissolved gas is equal to C_{bulk}. Therefore, C can be

Author's personal copy

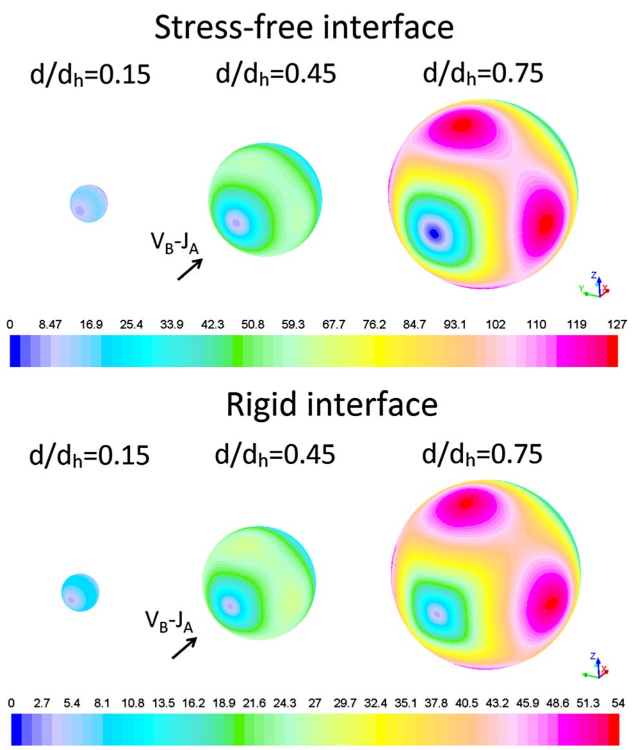

Fig. 14 Contour plots of $\mathrm{Sh}_{\mathrm{loc}}$ on the bubble surface, for various d/d_h, with a stress-free or a rigid interface, $\mathrm{Re}_{J_A} = 28.7$ and $\mathrm{Sc} = 551.3$, in the case of the square microchannel (color figure online)

locally higher or lower than C_{bulk} on this plane (depending of the influence of the preceding bubble on the concentration field) and in a cross section of the square or circular microchannel; C^* can thus be locally lower than 0, as observed in Figs. 11 and 13. For the square microchannel, C^* is lower than 0 in the wedges, as shown in Fig. 11 for $d/d_h = 0.75$. In Figs. 11 and 13, it can also be seen that C is higher than C_{bulk} ($C^* > 0$) at the central region of the IN plane.

4.4 Local mass transfer between a bubble and the surrounding liquid

The mass transfer rate between the bubble and the surrounding liquid is characterized locally on the bubble surface by defining a local Sherwood number as

$$\mathrm{Sh}_{\mathrm{loc}} = \frac{d\,\mathbf{n}\cdot\nabla C}{C_{\mathrm{int}} - C_{\mathrm{bulk}}}. \tag{23}$$

In Fig. 14, $\mathrm{Sh}_{\mathrm{loc}}$ is presented on the bubble surface for various d/d_h, with $\mathrm{Re}_{J_A} = 28.7$ and $\mathrm{Sc} = 551.3$, in the case of the square microchannel, with either a stress-free or a rigid interface.

The contour plots of $\mathrm{Sh}_{\mathrm{loc}}$ in Fig. 14 show that the highest mass transfer rate is observed at a position on the bubble surface characterized by $0 < \theta < \pi/2$. In Fig. 15, $\mathrm{Sh}_{\mathrm{loc}}$ is presented versus θ in the symmetry plane $z = 0$ of the square and circular microchannels, for various d/d_h, $\mathrm{Re}_{J_A} = 28.7$, $\mathrm{Sc} = 551.3$ and with either a stress-free or a rigid interface. In Fig. 15, for each considered value of d/d_h, $\mathrm{Sh}_{\mathrm{loc}}$ is also presented versus θ for a bubble rising in an infinite liquid medium, with either a stress-free or a rigid interface, with a Schmidt number $\mathrm{Sc} = 551.3$ and with a Reynolds number $\mathrm{Re}_\infty = \mathrm{Re}_{J_A}(\frac{V_B}{J_A} - 1)\frac{d}{d_h}$, with $\mathrm{Re}_{J_A} = 28.7$ and $\frac{V_B}{J_A}$ given as a function of d/d_h using Tables 6 and 7 in "Appendix 2." These $\mathrm{Sh}_{\mathrm{loc}}$ for a single bubble in an infinite medium are calculated using the following equations, developed by Levich (1962) for low Reynolds numbers:

Stress-free interface:

$$\mathrm{Sh}_{\mathrm{loc}} = \sqrt{\frac{3}{\pi}}(\mathrm{Re}_\infty \mathrm{Sc})^{1/2}\frac{1+\cos\theta}{\sqrt{2+\cos\theta}} \quad \text{(infinite medium)} \tag{24}$$

Rigid interface:

$$\mathrm{Sh}_{\mathrm{loc}} = \frac{1}{1.15}(3\mathrm{Re}_\infty \mathrm{Sc})^{1/3}\frac{\sin\theta}{\left(\theta - \frac{\sin 2\theta}{2}\right)^{1/3}} \quad \text{(infinite medium)} \tag{25}$$

Even though these correlations are not rigorously applicable for moderate Reynolds numbers and for a chain of bubbles, we use them here for qualitative comparison purpose. For both stress-free and rigid interfaces, the bubble velocity V_B used for evaluating Re_∞, and thus $\mathrm{Sh}_{\mathrm{loc}}$ in the infinite medium, is the one evaluated in the square microchannel.

At the front of the bubble, $\mathrm{Sh}_{\mathrm{loc}}$ is the highest for a bubble moving in an infinite medium while it is low for a bubble moving in microchannels. In the infinite medium, the highest mass transfer rate is observed at the front of the bubble because the diffusion boundary layer is the thinnest there. In the microchannels, $\mathrm{Sh}_{\mathrm{loc}}$ is low at the front of the bubble because the recirculation present in the liquid phase creates a convergent stagnation region and because the liquid impacting the front of the bubble has C larger than C_{bulk} due to the preceding bubble (see Figs. 11 and 13). The convergent stagnation region is a region where the liquid flow converges. It leads to a region with a thick diffusion boundary layer and thus a low $\mathrm{Sh}_{\mathrm{loc}}$. It is worth mentioning that a stagnation region also exist at the front of a bubble moving in an infinite medium, but it is a divergent stagnation point (Bird et al. 2007). The liquid flow diverges from this point and leads to a thin diffusion boundary layer and thus to a high $\mathrm{Sh}_{\mathrm{loc}}$. For the bubble with a stress-free interface in the microchannels, $\mathrm{Sh}_{\mathrm{loc}}$ at the front of the bubble increases when d/d_h decreases because the recirculation vanishes, the concentration of the dissolved gas in the liquid impacting the front of the bubble due to the preceding bubble decreases and the velocity around the bubble surface increases. For the bubble with a rigid interface, as, in the considered cases, the

Author's personal copy

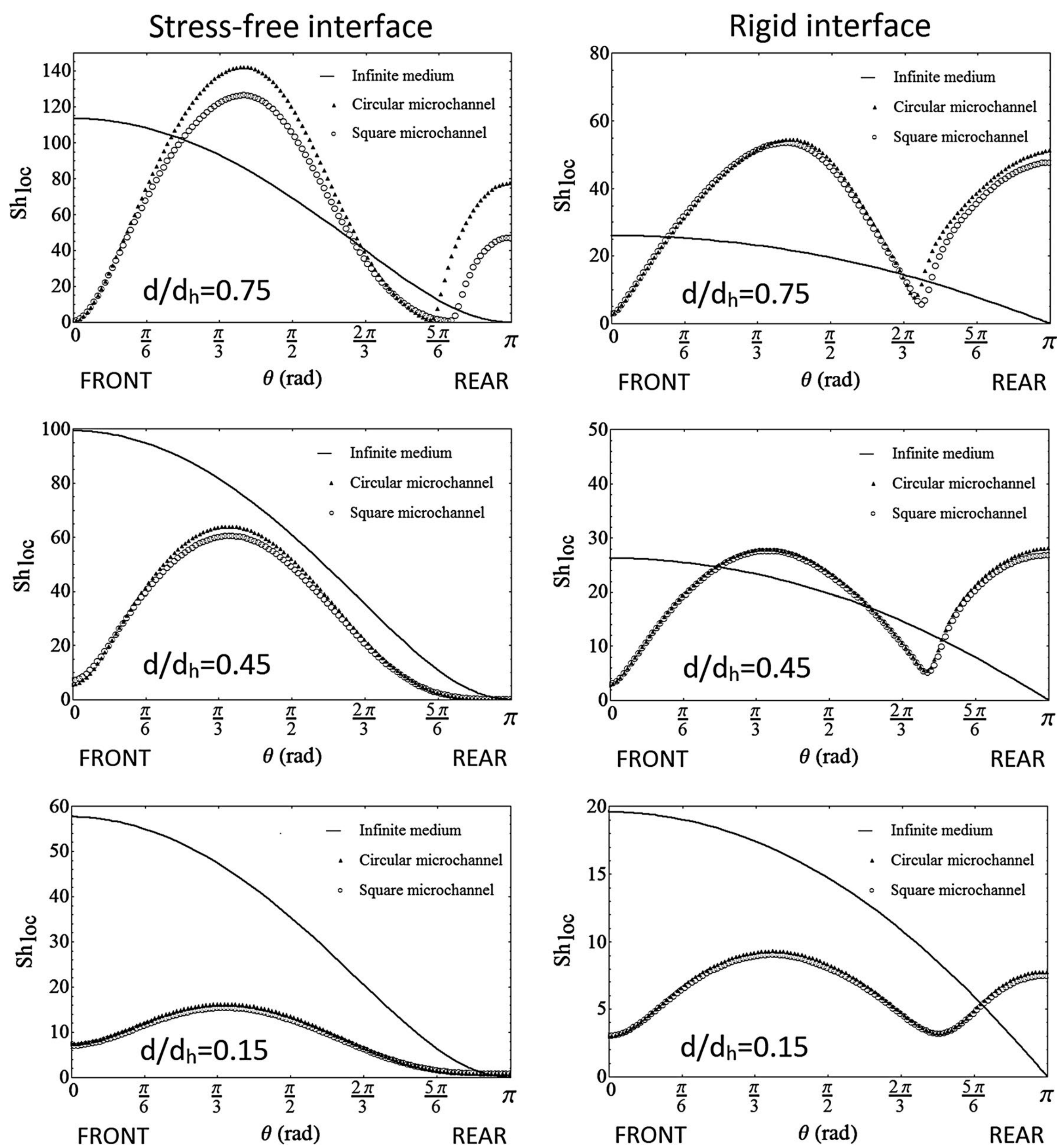

Fig. 15 Plots of $\mathrm{Sh}_{\mathrm{loc}}$ versus θ on the bubble surface in the symmetry plane $z = 0$. The results are presented for a stress-free or a rigid interface, in the square and circular microchannels, for $\mathrm{Re}_{J_A} = 28.7$ and $\mathrm{Sc} = 551.3$, as well as in an infinite medium

recirculation does not vanish when d/d_h decreases, the convergent stagnation point at the front of the bubble remains too and an increase of $\mathrm{Sh}_{\mathrm{loc}}$ is not observed there.

In microchannels, the highest $\mathrm{Sh}_{\mathrm{loc}}$ is observed at a position on the bubble surface characterized by $\theta \approx \pi/3$ because the diffusion boundary layer is the thinnest in this region. For $d/d_h = 0.75$ in the case of the bubble with a stress-free interface and for $d/d_h = 0.75$ and $d/d_h = 0.45$ in the case of the bubble with a rigid interface, $\mathrm{Sh}_{\mathrm{loc}}$ is even higher in this region for a bubble in a microchannel than in an infinite medium.

When a recirculation is present between two successive bubbles, it helps cleaning the bubble-liquid interface at the rear of the bubble and a substantial mass transfer is then present there. This recirculation vanishes when d/d_h decreases in the case of the bubble with a stress-free interface, while it is present for each analyzed value of d/d_h in the case of the bubble with a rigid interface. Therefore, when d/d_h decreases, the mass transfer rate between the bubble and the surrounding liquid at the rear of the bubble almost vanishes in the case of the bubble with a stress-free interface, while it remains substantial in the case of the bubble with a rigid interface.

Author's personal copy

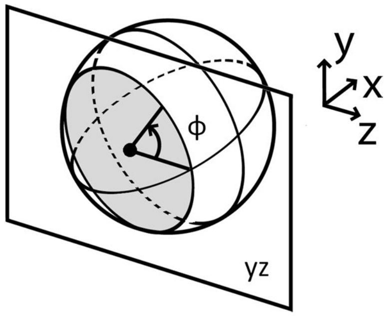

Fig. 16 Intersection between the bubble surface and the plane *yz* passing through the constant *x* position where the maximum value of $\mathrm{Sh}_{\mathrm{loc}}$ is observed, with • the center of the circle resulting from this intersection, and definition of the angle ϕ

Except at the front of the bubble, the mass transfer rate on the bubble surface is higher in the circular than in the square microchannel, at fixed values of d/d_h, Re_{J_A} and Sc. This was expected because, for square and circular microchannels with the same hydraulic diameter, the fraction of the area of the microchannel cross section available in the plane $x = 0$ for the liquid flow around a bubble is lower in the circular than in the square microchannel; the dimensionless velocity magnitude around the bubble and the subsequent mass transfer rate are then higher in the circular microchannel. When d/d_h decreases, $\mathrm{Sh}_{\mathrm{loc}}$ is almost the same in both types of microchannel because the difference of dimensionless velocity magnitude decreases.

As it can be observed in Fig. 14, when d/d_h increases, the azimuthal asymmetry of the local mass transfer rate on the bubble surface in the square microchannel becomes more pronounced. In order to analyze quantitatively this observation, the plane *yz*, passing through the constant *x* position where the maximum value of $\mathrm{Sh}_{\mathrm{loc}}$ is observed, is defined in Fig. 16, together with the angle ϕ corresponding to the azimuthal angle on this plane, with its origin taken at the intersection between the planes *yz* and $y = 0$.

In Fig. 17, $\mathrm{Sh}_{\mathrm{loc}}$ is presented versus ϕ in the plane *yz* of the square microchannel, for various d/d_h, with $\mathrm{Re}_{J_A} = 28.7$, $\mathrm{Sc} = 551.3$ and either a stress-free or a rigid interface. The azimuthal asymmetry of $\mathrm{Sh}_{\mathrm{loc}}$ is present because of the azimuthal asymmetry of the liquid flow mentioned in Sect. 4.2, which leads to a thinner diffusion boundary layer on the bubble surface in the symmetry planes $y = 0$ and $z = 0$ than between them and thus to a higher $\mathrm{Sh}_{\mathrm{loc}}$ in the symmetry planes than between them. When d/d_h decreases, the azimuthal asymmetry of the mass transfer rate on the bubble surface becomes less pronounced because the liquid velocity next to the bubble surface is almost the same in the symmetry planes than between them (see Sect. 4.2).

5 Conclusions and perspectives

In this paper, a numerical procedure is developed in order to analyze the liquid flow and the mass transport around a spherical bubble in square and circular microchannels, in the bubbly flow regime. A one-sided approach, where only the liquid flow is considered, is applied, and pseudo-periodic conditions are used in order to mimic the chain of bubbles encountered in real microchannels. Two limiting cases are considered regarding the gas–liquid interface: a stress-free interface or a rigid interface. The results enable correlations to be established in order to express V_B/J_A and Sh as functions of the dimensionless control parameters of the analyzed system in both types of microchannels and for both types of boundary conditions at the bubble–liquid interface. The analysis of the liquid flow around the bubble shows that a recirculation can be present between two successive bubbles depending on d/d_h and the boundary condition at the bubble–liquid interface. Indeed, for a bubble with a stress-free interface, this recirculation is observed only for values of d/d_h close to unity, while for a bubble with a rigid interface, it is observed for all the considered values of d/d_h. The analysis of the mass transport around the bubble highlights the influence of the liquid flow on the mass transport around the bubble in all the cases considered in this work. Indeed, this analysis points out that the highest mass transfer rates are observed at a position on the bubble surface characterized by $\theta \approx \pi/3$, where the liquid flow generates the thinnest diffusion boundary layer. It also shows that, when a recirculation is present between two successive bubbles, the mass transfer rate is low at the front of the bubble, due to the presence of a convergent stagnation point, while it is substantial at its rear, where a divergent stagnation point is observed.

When the flow and the mass transport around a bubble with a stress-free or a rigid interface in square and circular microchannels are analyzed, the main difference between the two types of microchannels is the presence, in the square microchannel, of an azimuthal asymmetry of the velocity field in the vicinity of the bubble surface, which leads to an azimuthal asymmetry of the mass transfer rate on the bubble surface. This asymmetry vanishes when d/d_h decreases.

The local mass transfer rate on the surface of a bubble with a stress-free or a rigid interface in a microchannel is compared with the local mass transfer on the surface of a bubble in an infinite liquid medium (for an equivalent Reynolds number and identical Sc). The results show that the local mass transfer rate on the surface of a bubble with a stress-free or a rigid interface can be higher or lower in a microchannel depending on the presence or not of a recirculation and on the heterogeneity of the dissolved gas

Author's personal copy

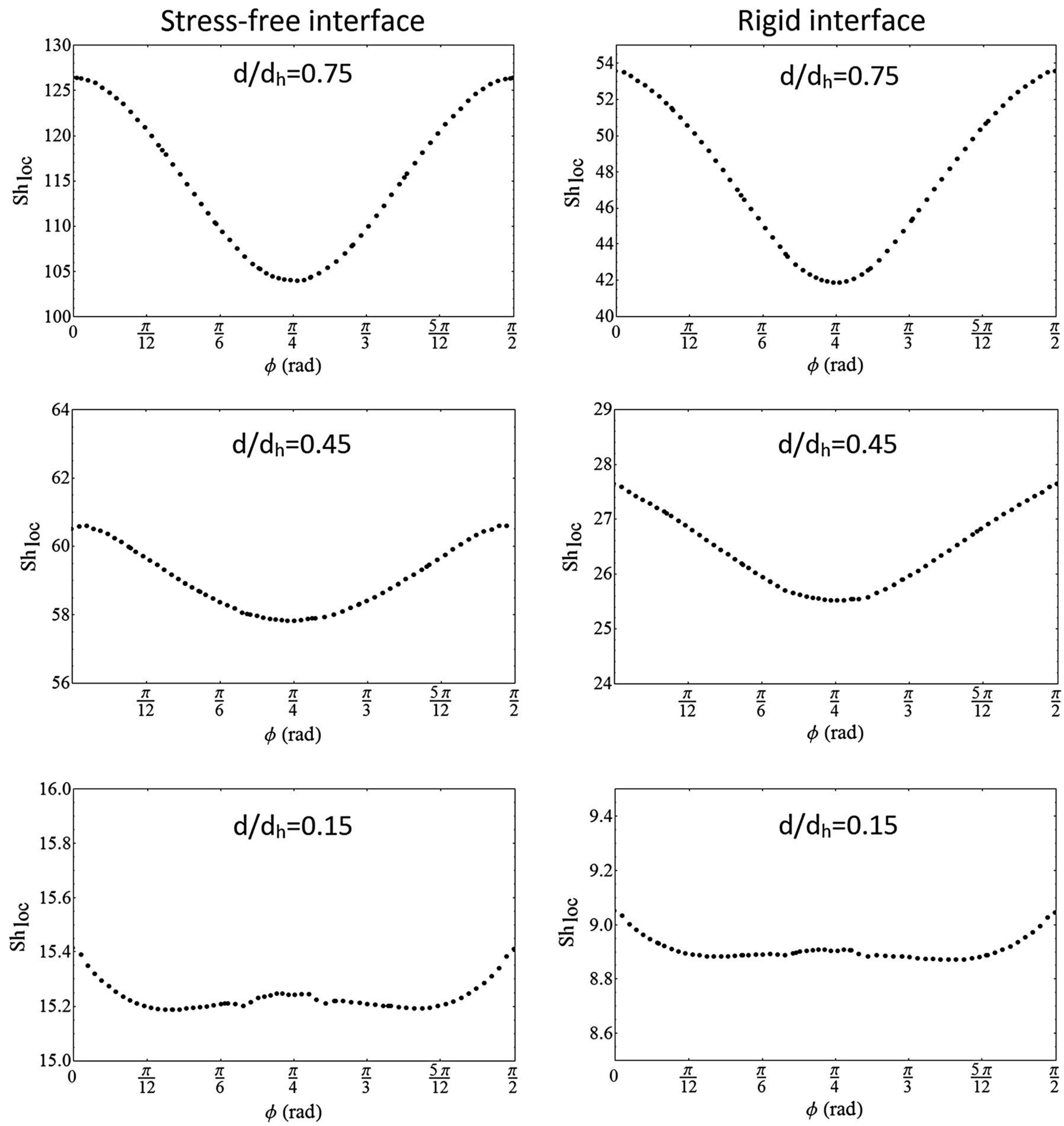

Fig. 17 Plots of Sh_{loc} versus ϕ on the bubble surface in the plane yz for $Re_{J_A} = 28.7$ and $Sc = 551.3$. The results are presented for a stress-free or a rigid interface, in the square microchannel. One-fourth of the microchannel is considered due to symmetries

concentration in the liquid entering the considered microchannel segment, due to the preceding bubble.

It was supposed in this work that the bubble is at the center of the microchannel. This hypothesis can be tested by making three-dimensional numerical simulations of the liquid flow for a complete square or circular microchannel segment containing a bubble slightly shifted vertically and horizontally relative to the microchannel center, and by analyzing whether the forces acting on the bubble surface will bring the bubble back toward the center. If the hypothesis is shown to be inappropriate, an equilibrium position of this bubble can be determined using a similar approach to the one used to determine V_B, and based on this position, new numerical simulations can be carried out for the analysis of the liquid flow and mass transport around the bubble.

As it is difficult to fabricate, experimentally, perfectly square microchannels, it could be interesting to extend the numerical procedure used here for the analysis of the liquid flow and the mass transport around a spherical bubble in square and circular microchannels to rectangular microchannels. In the same view, one could extend our numerical procedure to the case of bubble chains with a separating distance L between bubbles smaller than the value for

Author's personal copy

which we have shown that it has no influence on the calculated values for V_B and Sh.

It is observed, in Fig. 6, that the bubble velocity evaluated experimentally by Cubaud et al. (2012) is comprised between the values of V_B that can be computed using the two limiting cases of the bubble with a stress-free and a rigid interface. It suggests that the liquid could have been contaminated in these experiments leading to a partially rigid interface. This observation could be used in order to evaluate the contamination level of a liquid in a microchannel by comparing the velocity of bubbles moving in this liquid to the velocities expected in the cases of bubbles with a stress-free or a rigid interface.

As mentioned above, the comparison between the correlations expressing the bubble velocity as a function of the bubble diameter in the square microchannel and the experimental data of Cubaud et al. (2012) suggests that, in these experiments, the liquid is partially contaminated. A "multiple stagnant caps" model could be used in order to investigate this possibility (see Wylock et al. 2011 for a description of the single stagnant cap model). In such a model, a no-slip condition would be used on the parts of the interface close to the stagnation points identified in Figs. 8 and 10 and a stress-free condition would be used for the other parts of the interface. The area of the parts of the interface where the no-slip condition is applied could then be varied, and its influence on the bubble velocity could be analyzed. Another possibility to model the partial contamination of the bubble-liquid interface could be to consider the transport of surfactants on the interface and in the liquid phase and to couple the boundary condition at the bubble surface to the concentration of surfactants on the bubble-liquid interface.

The lack of experimental data regarding the dissolution of bubbles along square and circular microchannels in the bubbly flow regime with a controlled contamination level of their interface is appealing for new experiments. The results of these experiments would not only enable a validation of the correlations expressing the bubble velocity and Sherwood number as functions of the control parameters of the system, at least for a clean—i.e., stress-free—interface, but would also provide a better insight on the surface (partial) rigidity of the bubbles traveling along microchannels.

The evolution of the size of a bubble was monitored in the bubbly flow regime along a nearly square microchannel in Cubaud et al. (2012), but a model for the dissolution of a spherical bubble, in a liquid, along a square or a circular microchannel in the bubbly flow regime has not been proposed yet. It is thus relevant to develop such a model and compare, in the case of a square microchannel, the calculated evolution of the bubble size along the microchannel to the data presented in Cubaud et al. (2012).

Acknowledgments The authors gratefully acknowledge Louise De Cannière for her assistance in numerical simulations. The authors also acknowledge Jean-Christophe Baret, Charles Baroud and Pierre Miquel for fruitful discussions. D.M. and B.S. acknowledge the Fonds de la Recherche Scientifique (F.R.S.–F.N.R.S.) for its financial support. This research has been performed under the umbrella of the COST action MP1106 and also took part in the Inter-university Attraction Pole Programme (IAP 7/38 MicroMAST) initiated by the Belgian Science Policy Office.

Appendix 1: Grid

Square microchannel

The geometry of the square microchannel is shown in Fig. 2. The principal volume is constituted of 5 subvolumes: Vol1, Vol2, Vol3, Vol4 and a zone Vol5 around the bubble. This principal volume is surrounded by smaller volumes forming a layer. These small volumes are referred to as V_{layer} hereafter. The meshing parameters of the edges presented in Fig. 2 are provided in Table 4. When an edge mentioned in Table 4 is meshed, the same mesh is applied to the other edges presented in Fig. 2, which are parallel to it and of the same length. Numerical values of the meshing parameters presented in Table 4 are provided in Table 5. For the edge cr, the number of intervals is calculated such

Table 4 Meshing parameters of the edges presented in Fig. 2

Edge	Length	Meshing scheme	Number of intervals	Size of the intervals	First length 1	First length 2
ext	L_0	Uniform	/	lext	/	/
ext2	$L - 2L_0$	Uniform	/	lext2	/	/
cr	Δ	First length	ncr	/	lcr	/
int	$(L - 2L_0)/2 - d/2 - \Delta$	Uniform	/	lext2	/	/
int2	$(L - 2L_0)/2$	Uniform	/	lext2	/	/
cc	/	Uniform	ncc	/	/	/
layer	llayer	Uniform	nlayer	/	/	/
side	$d_h/2$ − llayer	Double-sided mesh	nside	/	lside	lside
ac	$d_h/2$ − llayer − Δ − d/2	Double-sided mesh	nmac	/	5lcr at the bubble side	lside at the wall side

Author's personal copy

Table 5 Numerical values of the parameters used for creating and meshing the edges presented in Table 4

d (μm)	d_h (μm)	L (μm)	L_0 (μm)	llayer (μm)	Δ (μm)	nlayer	lext (μm)	lext2 (μm)	nside	lside (μm)	ncc	lcr (μm)	ncr	nmac
150	200	5000	1600	1.6	10	4	5	2.5	76	0.398	60	0.302	15	20
130		4800	1500		10				78			0.267	15	30
110		4400	1200		10				78			0.238	17	50
90		4300	1100		10				74			0.219	19	60
70		4200	1000		10				70			0.196	21	60
50		3600	900		10				80			0.163	25	60
30		2000	400		2				110			0.096	9	70

that the ratio of the size of the last interval to the size of the first interval does not exceed 5.

Once the edges are meshed, Vol1, Vol4 and V_{layer} are meshed using Hex(ahedral) elements of type Map. It enables having the same mesh on the planes IN and OUT, which is necessary for using pseudo-periodic boundary conditions. Vol5 is meshed using Hex/Wedge elements and Vol2 and Vol3 are meshed using Tet(rahedral) elements. The Tet(rahedral) elements of Vol2 and Vol3 are combined in order to form polyhedra. It enables reducing the number of elements, improving the quality of the mesh and fastening the convergence.

V_{layer} and Vol5 are used in order to accurately capture the diffusion boundary layers at the walls of the microchannel and at the bubble surface, as explained in Sect. 3.1.

Circular microchannel

The two-dimensional geometry used for the circular microchannel is shown in Fig. 3. The principal surface is divided in 5 subsurfaces: S1, S2, S3, S4 and a surface S5 around the bubble. Smaller surfaces forming a layer are present at the top of the principal surface. These small surfaces are referred to as S_{layer} hereafter. S_{layer} and S5 are used in order to accurately capture the diffusion boundary layers at the walls of the microchannel and at the bubble surface. The edges have the same names as for the square microchannel and are created and meshed in the same way as described in "Square microchannel" in Appendix 1. Once the edges are meshed, S1, S4, S5 and S_{layer} are meshed using Quad(rilateral) elements and S2 and S3 using Tri(angular) elements.

Table 6 Values of the dimensionless control parameters and the postprocessed parameters for all the numerical simulations of the flow and the mass transport around the bubble with a stress-free interface in the square microchannel, with $\text{Re} = \text{Re}_{J_A} \frac{V_B}{J_A} \frac{d}{d_h}$

d/d_h	Re_{J_A}	V_B/J_A	Re	Sh (Sc = 152)	Sh (Sc = 356)	Sh (Sc = 551.3)
0.15	28.70	2.098	9.03	6.30	8.46	9.93
	17.22	2.095	5.41	5.31	6.97	8.12
	5.74	2.088	1.80	3.89	4.81	5.45
0.25	28.70	2.101	15.07	11.44	15.98	18.94
	17.22	2.100	9.04	9.38	13.05	15.50
	5.74	2.100	3.01	6.32	8.55	10.09
0.35	28.70	2.103	21.12	17.42	24.10	28.21
	17.22	2.100	12.65	14.18	19.81	23.39
	5.74	2.100	4.22	9.21	12.86	15.30
0.45	28.70	2.088	26.96	23.37	31.40	35.97
	17.22	2.087	16.17	19.26	26.42	30.66
	5.74	2.086	5.39	12.44	17.48	20.72
0.55	28.70	2.056	32.45	29.54	38.67	43.64
	17.22	2.052	19.43	24.57	33.08	37.89
	5.74	2.050	6.47	15.91	22.36	26.34
0.65	28.70	1.982	36.97	36.72	48.07	54.32
	17.22	1.976	22.11	30.52	41.18	47.16
	5.74	1.973	7.36	19.51	27.72	32.75
0.75	28.70	1.851	39.84	45.05	59.89	68.55
	17.22	1.845	23.82	37.20	50.80	58.62
	5.74	1.841	7.92	23.26	33.67	40.06

Author's personal copy

Appendix 2: Numerical results

The values of the dimensionless control parameters and the postprocessed parameters are presented in Tables 6, 7, 8 and 9 for all the numerical simulations of the flow and the mass transport around the bubble with a stress-free or a rigid interface in the square or the circular microchannel.

Table 7 Values of the dimensionless control parameters and the postprocessed parameters for all the numerical simulations of the flow and the mass transport around the bubble with a rigid interface in the square microchannel

d/d_h	Re_{J_A}	V_B/J_A	Re	Sh (Sc = 152)	Sh (Sc = 356)	Sh (Sc = 551.3)
0.15	28.70	2.069	8.91	4.76	5.88	6.66
	17.22	2.070	5.35	4.28	5.16	5.77
	5.74	2.069	1.78	3.52	4.08	4.44
0.25	28.70	2.022	14.51	7.39	9.59	10.96
	17.22	2.022	8.70	6.33	8.19	9.37
	5.74	2.022	2.90	4.77	5.90	6.69
0.35	28.70	1.950	19.58	10.24	13.29	15.16
	17.22	1.951	11.76	8.72	11.35	12.96
	5.74	1.951	3.92	6.23	8.06	9.24
0.45	28.70	1.859	24.01	13.11	16.93	19.29
	17.22	1.860	14.41	11.18	14.49	16.51
	5.74	1.861	4.81	7.91	10.34	11.83
0.55	28.70	1.750	27.62	16.08	20.75	23.65
	17.22	1.751	16.58	13.73	17.76	20.24
	5.74	1.752	5.53	9.69	12.70	14.53
0.65	28.70	1.627	30.35	19.32	24.99	28.53
	17.22	1.628	18.22	16.48	21.39	24.40
	5.74	1.629	6.08	11.58	15.23	17.46
0.75	28.70	1.498	32.24	22.86	29.65	33.92
	17.22	1.497	19.33	19.44	25.32	28.93
	5.74	1.497	6.44	13.60	17.95	20.62

Table 8 Values of the dimensionless control parameters and the postprocessed parameters for all the numerical simulations of the flow and the mass transport around the bubble with a stress-free interface in the circular microchannel

d/d_h	Re_{J_A}	V_B/J_A	Re	Sh (Sc = 152)	Sh (Sc = 356)	Sh (Sc = 551.3)
0.15	28.70	2.003	8.62	6.66	8.99	10.57
	17.22	2.003	5.17	5.64	7.47	8.74
	5.74	2.003	1.72	4.15	5.23	5.98
0.25	28.70	2.005	14.38	12.14	17.00	20.14
	17.22	2.005	8.63	9.94	13.89	16.52
	5.74	2.005	2.88	6.63	9.04	10.70
0.35	28.70	2.001	20.10	18.51	25.65	29.94
	17.22	2.000	12.05	15.07	21.14	24.95
	5.74	2.000	4.02	9.70	13.64	16.28
0.45	28.70	1.981	25.58	25.22	34.02	38.90
	17.22	1.980	15.34	20.69	28.58	33.22
	5.74	1.979	5.11	13.18	18.72	22.28
0.55	28.70	1.928	30.43	32.38	42.98	48.61
	17.22	1.925	18.23	26.66	36.50	42.07
	5.74	1.923	6.07	16.89	24.14	28.68
0.65	28.70	1.819	33.93	41.27	55.53	63.22
	17.22	1.815	20.31	33.69	46.83	54.35
	5.74	1.812	6.76	20.68	30.33	36.40
0.75	28.70	1.640	35.30	52.21	72.54	84.28
	17.22	1.637	21.14	41.80	59.98	70.76
	5.74	1.636	7.04	24.66	37.27	45.51

Author's personal copy

Table 9 Values of the dimensionless control parameters and the postprocessed parameters for all the numerical simulations of the flow and the mass transport around the bubble with a rigid interface in the circular microchannel

d/d_h	Re_{J_A}	V_B/J_A	Re	Sh (Sc = 152)	Sh (Sc = 356)	Sh (Sc = 551.3)
0.15	28.70	1.970	8.48	4.93	6.13	6.96
	17.22	1.970	5.09	4.42	5.36	6.01
	5.74	1.970	1.70	3.61	4.20	4.60
0.25	28.70	1.916	13.75	7.72	10.03	11.46
	17.22	1.916	8.25	6.60	8.56	9.79
	5.74	1.917	2.75	4.92	6.14	6.98
0.35	28.70	1.837	18.45	10.74	13.94	15.88
	17.22	1.838	11.08	9.15	11.91	13.60
	5.74	1.838	3.69	6.49	8.45	9.69
0.45	28.70	1.736	22.42	13.85	17.91	20.38
	17.22	1.737	13.46	11.79	15.33	17.48
	5.74	1.737	4.49	8.29	10.90	12.50
0.55	28.70	1.617	25.52	17.16	22.21	25.29
	17.22	1.618	15.32	14.60	19.02	21.70
	5.74	1.618	5.11	10.20	13.49	15.50
0.65	28.70	1.485	27.70	20.87	27.19	31.08
	17.22	1.485	16.62	17.69	23.21	26.57
	5.74	1.485	5.54	12.25	16.30	18.81
0.75	28.70	1.346	28.97	25.09	33.04	37.97
	17.22	1.346	17.38	21.15	28.03	32.26
	5.74	1.346	5.79	14.47	19.44	22.54

References

Bruus H (2008) Theoretical microfluidics, vol 18. Oxford University Press, Oxford, pp 41–50 and 75

Bird RB, Stewart WE, Lightfoot EN (2007) Transport phenomena. Wiley, New York, pp 100, 636 and 677–678

Champougny L, Scheid B, Restagno F, Vermant J, Rio E (2015) Surfactant-induced rigidity of interfaces: a unified approach to free and dip-coated films. Soft Matter 11:2758–2770

Clift R, Grace JR, Weber ME (1978) Bubbles, drops and particles. Academic Press, New York

Coulson JM, Richardson JF (1991) Chemical engineering volume 2: particle technology and separation, 4th edn. Pergamon Press, Oxford

Cubaud T, Ho CM (2004) Transport of bubbles in square microchannels. Phys Fluids 16:4575

Cubaud T, Sauzade M, Sun R (2012) CO_2 dissolution in water using long serpentine microchannels. Biomicrofluidics 6:022002

Dani A, Cockx A, Guiraud P (2006) Direct numerical simulation of mass transfer from spherical bubbles: the effect of interface contamination at low Reynolds numbers. Int J Chem React Eng 4(1):1542

Figueroa-Espinoza B, Legendre D (2010) Mass or heat transfer from spheroidal gas bubbles rising through a stationary liquid. Chem Eng Sci 65:6296–6309

Haas U, Schmidt-Traub H, Brauer H (1972) Umströmung kugelförmiger Blasen mit innerer Zirkulation. Chem Ing Tech 44:1060–1068

Haberman WL, Morton RK (1953) An experimental investigation of the drag and shape of air bubbles rising in various liquids. David Taylor Model Basin, Report 802

Haut B, Colinet P (2005) Surface-tension-driven instabilities of a pure liquid layer evaporating into an inert gas. J Colloid Interface Sci 285:296–305

Kashid MN, Renken A, Kiwi-Minsker L (2011) Gas–liquid and liquid–liquid mass transfer in microstructured reactors. Chem Eng Sci 66(17):3876–3897

Kawahara A, Chung PY, Kawaji M (2002) Investigation of two-phase flow pattern, void fraction and pressure drop in a microchannel. Int J Multiph Flow 28(9):1411–1435

Kim N, Evans ET, Park DS, Soper SA, Murphy MC, Nikitopoulos DE (2011) Gas–liquid two-phase flows in rectangular polymer micro-channels. Exp Fluids 51(2):373–393

Levich VG (1962) Physicochemical hydrodynamics, vol 689. Prentice-Hall, Englewood Cliffs, NJ, pp 84–85 and 467

Magnaudet J, Rivero M, Fabre J (1995) Accelerated flows past a rigid sphere or a spherical bubble. Part 1. J Fluid Mech 284:97–135

Mikaelian D, Haut B, Scheid B (2015) Bubbly flow and gas-liquid mass transfer in square and circular microchannels for stress-free and rigid interfaces: dissolution model. Microfluid Nanofluid (in revision)

Pamme N (2007) Continuous flow separations in microfluidic devices. Lab Chip 7(12):1644–1659

Ponoth SS, McLaughlin JB (2000) Numerical simulation of mass transfer for bubbles in water. Chem Eng Sci 55:1237–1255

Ratulowski J, Chang HC (1990) Marangoni effects of trace impurities on the motion of long gas bubbles in capillaries. J Fluid Mech 210:303–328

Rust AC, Manga M (2002) Bubble shapes and orientations in low Re simple shear flow. J Colloid Interface Sci 249(2):476–480

Shim S, Wan J, Hilgenfeldt S, Panchal PD, Stone HA (2014) Dissolution without disappearing: multicomponent gas exchange for CO_2 bubbles in a microfluidic channel. Lab Chip 14:2428–2436

Song H, Chen DL, Ismagilov RF (2006) Reactions in droplets in microfluidic channels. Angew Chem Int Edn 45(44):7336–7356

Stebe KJ, Barthès-Biesel D (1995) Marangoni effects of adsorption-desorption controlled surfactants on the leading end of an infinitely long bubble in a capillary. J Fluid Mech 286:25–48

Author's personal copy

Sun R, Cubaud T (2011) Dissolution of carbon dioxide bubbles and microfluidic multiphase flows. Lab Chip 11(17):2924–2928

Triplett KA, Ghiaasiaan SM, Abdel-Khalik SI, Sadowski DL (1999a) Gas–liquid two-phase flow in microchannels part I: two-phase flow patterns. Int J Multiph Flow 25(3):377–394

Triplett KA, Ghiaasiaan SM, Abdel-Khalik SI, LeMouel A, McCord BN (1999b) Gas–liquid two-phase flow in microchannels: part II: void fraction and pressure drop. Int J Multiph Flow 25(3):395–410

Wylock C, Larcy A, Colinet P, Cartage T, Haut B (2010) Direct numerical simulation of the CO_2 transfer from spherical bubbles to $NaHCO_3$ and Na_2CO_3 aqueous solutions with clean and fully contaminated interface. Colloids Surf A Physicochem Eng Asp 365:28–35

Wylock C, Larcy A, Colinet P, Cartage T, Haut B (2011) Direct numerical simulation of bubble–liquid mass transfer coupled with chemical reactions: influence of bubble shape and interface contamination. Colloids Surf A Physicochem Eng Asp 381:130–138